# Past and future ocean warming

*Lijing Cheng*[1,2]✉, *Karina von Schuckmann*[3], *John P. Abraham*[4], *Kevin E. Trenberth*[5,6], *Michael E. Mann*[7], *Laure Zanna*[8], *Matthew H. England*[9,10], *Jan D. Zika*[10,11], *John T. Fasullo*[5], *Yongqiang Yu*[1], *Yuying Pan*[1,2], *Jiang Zhu*[1,2], *Emily R. Newsom*[8], *Ben Bronselaer*[12] *and Xiaopei Lin*[13,14]

Abstract | Changes in ocean heat content (OHC) provide a measure of ocean warming, with impacts on the Earth system. This Review synthesizes estimates of past and future OHC changes using observations and models. The top 2,000 m of the global ocean has significantly warmed since the 1950s, gaining 351 ± 59.8 ZJ (1 ZJ = $10^{21}$ J) from 1958 to 2019. The rate of warming increased from <5 to ~10 ZJ $yr^{-1}$ from the 1960s to the 2010s. Observed area-averaged warming is largest in the Atlantic Ocean and southern oceans at 1.42 ± 0.09 and 1.40 ± 0.09 × $10^{9}$ J $m^{-2}$, respectively, for the upper 2,000 m over 1958–2019. These observed patterns of heat gains are dominated by heat redistribution. Observationally constrained projections suggest that historic ocean warming is irreversible this century, with net warming dependent on the emission scenario. By 2100, projected warming in the top 2,000 m is 2–6 times that observed so far, ranging from 1,030 [839–1,228] ZJ for a low-emission scenario to 1,874 [1,637–2,109] ZJ for a high-emission scenario. The Pacific is projected to be the largest heat reservoir owing to its size, but area-averaged warming remains strongest in the Atlantic and southern oceans. Ocean warming has extensive impacts that pose risks to marine ecosystems and society. The projected changes necessitate a continuation and improvement of observations and models, along with better uncertainty estimation.

Earth energy imbalance
EEI. The net downwelling radiation at the top of the atmosphere, represented as the balance of absorbed solar radiation (allowing for reflection and scattering) and outgoing longwave radiation.

Ocean heat content
OHC, or ocean heat storage (OHS). A change or anomaly of the thermal energy of the ocean assumed to have a fixed volume ($V_{x,y,z}$, in units of J), and vertical integration ($V_z$, in units of J $m^{-2}$). Calculated as $OHC(x,y,z) = C_p \iiint_{V(x,y,z)} \rho T dV(x,y,z)$ following TEOS-10 standards, where $c_p$ is a constant of ~3,991.9 J (kg K)$^{-1}$, $\rho$ is potential density in kg $m^{-3}$ and $T$ is conservative temperature measured in degrees Celsius.

✉e-mail: chenglij@mail.iap.ac.cn

https://doi.org/10.1038/s43017-022-00345-1

Increasing anthropogenic greenhouse gas (GHG) concentrations cause a positive Earth energy imbalance (EEI), with resulting surplus heat in the climate system increasing ocean heat content (OHC)[1–3] (FIG. 1a, F1). Unprecedented oceanic warming has been observed since at least the 1950s, reaching record values from 2012–2021 (REFS.[3,4]). This oceanic warming has been pervasive, spreading from the surface to the abyssal layers (each responding differently; BOX 1), and with the long-term OHC trend accelerating[5–8].

Owing to the large thermal inertia of the ocean, subsurface warming represents the slow response to external influences, in particular to GHG forcing (BOX 1). In response to past and current carbon emissions, future ocean warming is therefore committed for many centuries[5,9], and is related to the current acceleration of ocean warming[10] (FIG. 1a). For instance, under representative concentration pathway (RCP) 8.5, it is projected that the total upper-2,000-m OHC increase from 2017–2100 will be ~5–7 times that observed from 1970 to 2017 (REF.[6]). The irreversibility of this ocean warming on centennial timescales creates additional requirements for climate policy, particularly considering the widespread impacts[10,11].

Indeed, ocean warming has a multifaceted role in the Earth system via its links to the energy, water and carbon cycles, and resulting feedbacks (FIG. 1). For instance, the vast majority of radiative energy trapped by GHGs is ultimately absorbed at the ocean surface. Part of the energy is stored in the ocean, but this warming leads to increased longwave radiation and surface evaporation, cooling the ocean[12,13] (FIG. 1a, F2). Increased evaporation, in turn, leads to moistening of the atmosphere, released as latent heat during precipitation[14], invigorating the hydrological cycle[15] (FIG. 1a, F3). In response, the sea surface salinity pattern is amplified, with salty regions getting saltier and fresh regions getting fresher[16]. These temperature and salinity changes also alter ocean density and circulation, triggering global ocean heat uptake (OHU)[6,17]. Ocean warming also affects the Earth's surface albedo[18–20], and sea-ice and ice-sheet[21,22] melt processes, increasing OHU[11,23] (FIG. 1a, F4 and F5).

Ocean heat redistribution processes, including circulation, mixing and convection, eventually spread this additional heat to the ocean interior[24–26] (FIG. 1a, F6). With this heat, anthropogenic $CO_2$ is also absorbed and transported, leading to a synchronous increase of OHC and ocean acidification[27,28]. However, through increased stratification and reduced uptake capacity and efficiency, warming decreases the efficiency of the oceanic carbon sink, further enhancing atmospheric $CO_2$ and ocean warming, a positive feedback[28,29] (FIG. 1a, F7).

OHC trend
Or alternatively, OHC rate, or tendency. The time derivative of OHC (dOHC/d$t$), given in units of J yr$^{-1}$ or W m$^{-2}$.

Representative concentration pathway
RCP. The RCPs are scenarios of concentrations, and thereby emissions, of the full suite of greenhouse gases, aerosols and chemically active gases, as well as land use/land cover. In RCP2.6: radiative forcing peaks at ~3 W m$^{-2}$ and then declines, to be limited at 2.6 W m$^{-2}$ in 2100. In RCP4.5 and RCP8.5: the radiative forcing reaches ~4.5 W m$^{-2}$ and >8.5 W m$^{-2}$ in 2100, respectively.

Ocean heat uptake
OHU. The accumulated contribution of heat added into the ocean (heat gain) or removed from the ocean (heat loss) through heat fluxes at the air–sea, ice–sea and land–sea interfaces (in units of W m$^{-2}$). Globally, it is synonymous with 'OHC change, trend, rate, tendency'. Regionally, OHU and redistribution contribute to local OHC change.

Ocean heat redistribution
The transport of heat within the ocean without involving any net global ocean warming or cooling through advection, convection, eddy mixing and small-scale diffusion.

In addition, ocean ecosystems and biological processes are also affected by ocean warming, and these then alter the carbon uptake and storage[6,30]. Thus, ocean warming threatens the fundamental conditions that make the Earth conducive to sustaining life (FIG. 1), necessitating better understanding of its changes.

In this Review, we outline past and future ocean warming, its drivers and consequences. We begin by outlining the current ocean observing system for monitoring ocean warming, followed by discussion of contemporary global and regional OHC changes. To support adaptation and mitigation, model projections of ocean warming are then provided. The far-reaching consequences of ocean warming on physical, human and biological systems of the Earth system are subsequently outlined, before ending with a discussion of the remaining challenges and outlook for monitoring and understanding ocean warming.

## Observing and estimating OHC

The Global Ocean Observing System[31] (GOOS) is essential for providing reliable estimates of ocean warming. The GOOS instrument types, geographical coverage and post-processing techniques have evolved rapidly[32]. Originally, subsurface OHC observations relied on hydrographic measurements from Nansen bottles (dominating 1900–1940 GOOS), mechanical bathythermographs (MBTs; dominating within 1940–1970) and expendable bathythermographs (XBTs; dominating within 1970–2001)[32,33].

From 1999, however, the international Argo system of autonomous profiling floats revolutionized oceanographic observations, measuring the upper 2,000 m at unprecedented resolution, and dominating ocean observations since about 2005 (REFS.[34,35]). Currently, ~3,900 profiling floats constitute the array, providing a system to make near-global measurements of the Earth's open ocean[36], with a target resolution of one profile every 3° × 3° every 10 days. However, the Argo data are much more limited in polar areas, shallow and coastal regions, in some major current systems, including the Indonesian throughflow (ITF), and in the water column below 2,000 m. Because the Argo network has incomplete global coverage, the global upper-2,000-m OHC rates based on Argo-only products can underestimate the rate of change by 10–20%[37–39]. Deep Argo has been developed to better capture measurements at 4,000–6,000 dbar (REF.[40]) with a resolution target of one profile every 5° × 5° every 10 days[41]. So far, ~170 Deep Argo floats have been regionally implemented out of the necessary 1,200. At a minimum, Argo floats measure temperature and salinity, but are increasingly also measuring biological and chemical properties[42].

These Argo data are complemented by other observation platforms, including XBTs, MBTs, Nansen bottles, ship-based CTDs (conductivity–temperature–depth sensors), gliders and moored arrays, offering opportunities for OHC comparisons and data acquisition in regions where Argo does not operate. For instance, the global XBT network still provides continuous and high-resolution (eddy-resolving) temperature profile data along repeated transects and critical channels[43]. The Marine Mammals Exploring the Ocean Pole to Pole (MEOP) programme — which equips marine animals, primarily southern elephant seals or other pinnipeds, with measurement devices — has also provided 600,000 vertical profiles in high-latitude coastal regions since about 2004 (REF.[44]). Ice-tethered profilers offer further data in high latitudes, obtaining temperature and salinity profiles with excellent vertical resolution.

Synthesizing all these in situ measurements into estimates of OHC requires consideration of quality control, bias correction, gap-filling (mapping) and uncertainty[33,45]. For example, the first estimate of OHC indicated long-term ocean warming in the upper 3,000 m over 1948–1998, and a particularly warm period from the 1970s to the early 1980s[46,47] (Supplementary Table 1). However, this pronounced warm period was found to be a spurious consequence of systematic errors in XBT data[48], as similarly identified in MBT[49] and Argo data[50]. These data quality issues and error corrections must be taken into account (Supplementary Table 1). The mapping method — how a global map is created from incomplete and inhomogeneous observations — also introduces uncertainty[36,51,52]. Many mapping strategies based on an objective analysis approach result in a conservative bias toward low-magnitude changes by assuming no change in less-sampled regions[53–57] (Supplementary Table 1). In doing so, some OHC estimates exhibit unduly weak long-term trends[5,53,58]. Several methods have been proposed to resolve these mapping challenges arising from data scarcity, including: the use of model simulations to guide the reconstruction[59]; incorporating SST[60] and/or sea level information[61]; combining five years of data for a pentadal estimate[62]; and using machine learning[63] (Supplementary Table 1).

In addition to these direct methods to observe and estimate OHC, several alternative approaches are also available, each with their own limitations (Supplementary Table 1). Indirect methods can be used to infer OHC change from physical relationships between OHC and other variables[33,64,65]. For instance, altimetry and space gravimetry have been used since the early 2000s to estimate OHC based on a sea level budget constraint[64,66–68], and SST used based on an assumption that temperature

**Author addresses**

[1]Institute of Atmospheric Physics, Chinese Academy of Sciences, Beijing, China.
[2]Center for Ocean Mega-Science, Chinese Academy of Sciences, Qingdao, China.
[3]Mercator Ocean International, Toulouse, France.
[4]School of Engineering, University of St. Thomas, Minneapolis, MN, USA.
[5]National Center for Atmospheric Research, Boulder, CO, USA.
[6]Department of Physics, The University of Auckland, Auckland, New Zealand.
[7]Department of Meteorology and Atmospheric Science, Earth and Environmental Systems Institute, Pennsylvania State University, University Park, PA, USA.
[8]Courant Institute, New York University, New York, NY, USA.
[9]Climate Change Research Centre, University of New South Wales, Sydney, New South Wales, Australia.
[10]Australian Research Council (ARC) Centre for Excellence in Antarctic Science, University of New South Wales, Sydney, New South Wales, Australia.
[11]School of Mathematics and Statistics, University of New South Wales, Sydney, New South Wales, Australia.
[12]Independent researcher, London, UK.
[13]Frontier Science Center for Deep Ocean Multispheres and Earth System and Physical Oceanography Laboratory, Ocean University of China, Qingdao, China.
[14]Qingdao National Laboratory for Marine Science and Technology, Qingdao, China.

**a** Principal processes and feedback loops (F) linked to ocean warming

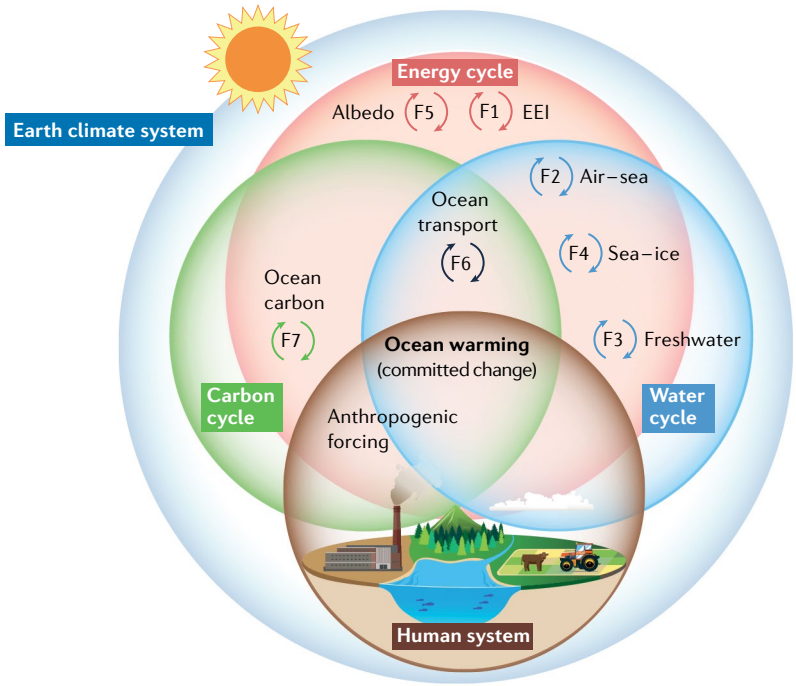


**b** Linkages of ocean warming to changes in the Earth system

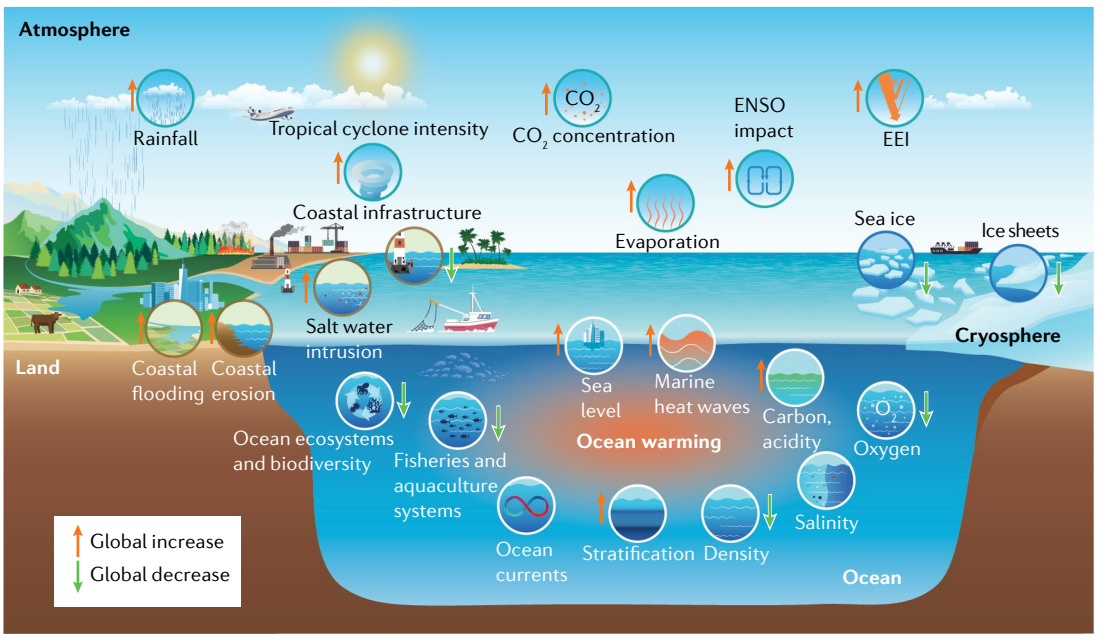


Fig. 1 | **The role of ocean warming in the climate system. a** | Principal processes and feedback loops (Fx) between ocean warming and physical and biogeochemical processes of the Earth system. The intersections between Earth system components indicates cycle and/or system coupling. **b** | Schematic representation of the linkage between ocean warming and multiple observed changes in the Earth system. Orange upward arrows indicate a global increase in the particular process, and green downward arrows a global decrease. Ocean warming is a key component of the Earth system, bridging key climate cycles and driving changes in Earth system processes and components.

anomalies behave as a passive tracer[69,70]. These indirect estimates rely on simplified assumptions, introduce additional uncertainty (Supplementary Table 1) and exhibit larger spread (FIG. 2), but can complement direct estimates.

Reanalyses can further be used to infer OHC change, wherein data assimilation of various observations constrains a model[71,72]. These ocean reanalyses produce 4D (latitude, longitude, depth and time) gridded estimates of all variables, making them very suitable for mechanistic research. However, most reanalyses do not conserve properties (for example heat and salt budget) during the assimilation step and so are not dynamically consistent[73,74]. Comparing these reanalysis datasets

Box 1 | **Surface and subsurface ocean warming**

The land, atmosphere and upper ocean (surface and mixed layer) respond relatively quickly (normally in years[206]) to surface radiative forcing, whereas the deep ocean typically adjusts over centuries to millennia[11]. Surface warming is approximately determined by cumulative emissions up to a given point in time, owing to a near-cancellation between the positive climate commitment and negative carbon cycle commitment[9,270]. This relationship implies that zero $CO_2$ emissions (assuming constant non-$CO_2$ emissions) lead to near-constant global surface temperature[270] — a finding that has critical implications for climate-change mitigation. However, the subsurface ocean responds far more slowly to anthropogenic forcing, in part owing to the slow nature of large-scale ocean circulation. Future subsurface ocean warming therefore has a much longer commitment time[9,11]. Even after net zero emissions are reached, the ocean subsurface will continue to warm as heat is transported downwards into deeper ocean waters, and a positive Earth energy imbalance remains until ocean and land carbon uptake sufficiently reduces atmospheric $CO_2$ concentrations. Ocean heat content (OHC) and sea level rise both integrate ocean temperature changes below the surface, and they continue to increase long after surface temperature stabilizes. This fundamental distinction between surface warming and OHC increases has important implications for both mitigation and adaptation strategies. Furthermore, as the measurements of sea surface temperatures (SSTs) rely on different instruments, the observations of SSTs are fundamentally different in their temporal and spatial coverage and temporal extent compared to subsurface observations and OHC estimates[271,272].

indicates substantial spread in OHC changes, implying that many are hampered by model and assimilation biases[75]. Yet reanalysis has the potential to be superior to objective analysis after ~2005 (with better consistency with top-of-atmosphere net radiation observations) after properly dealing with model and assimilation biases[76,77], but with large and spurious variability before this time[75] (Supplementary Fig. 1). Given that long-term changes are the focus of this Review, ocean reanalyses are therefore not included. Instead, subsequent discussion and analysis of OHC will focus on direct and indirect datasets that have complete bias correction and a valid evaluation procedure (Supplementary Table 1).

## OHC changes since the mid-twentieth century

Various estimates of OHC are available since 1957/1958 when a large amount of hydrographic data was collected for the International Geophysical Year[32,43,59]. Using three estimates that have been bias-corrected and have a valid evaluation procedure[59,60,62], global (approximately 80° S to 90° N) OHC changes at 0–700 m and 0–2,000 m over 1958–2020 are now described, as well as those at depths >2,000 m. To reduce the effects of high-frequency climate variability[76,78–80], a locally weighted scatterplot smoothing (LOWESS) approach is used to calculate mean warming rates[81] (Supplementary Information).

***Global upper-ocean change.*** Robust warming is apparent in the upper layers of the ocean since the late 1950s (FIG. 2a,c and TABLE 1). For instance, at 0–700 m, globally averaged OHC increased by 229.5 ± 33.8 ZJ (1 ZJ = $10^{21}$ J; ±1.64$\sigma$ error range represents the 90% confidence interval) from 1958 to 2019, equating to a mean ocean warming rate of 3.8 ± 0.6 ZJ $yr^{-1}$ (1 ZJ $yr^{-1}$ ≈ 0.062 W $m^{-2}$). Over 0–2,000 m, these OHC changes are larger, owing to a greater ocean volume, and reach 351.4 ± 59.8 ZJ over the same time period, equating to a mean ocean warming rate of 5.8 ± 1.0 ZJ $yr^{-1}$. These estimates are generally consistent with past quantifications (TABLE 1), albeit with some variability in trends and uncertainty owing to differences in data selection, trend estimates and methodological approaches[6,38,82] (Supplementary Information).

These warming rates have increased over time (FIG. 2b,d). For instance, OHC at 0–700 m increased from ~0–3.5 ZJ $yr^{-1}$ in the 1960s to ~4.8–8.0 ZJ $yr^{-1}$ by the 2010s. OHC at 0–2,000 m increased from ~0–4.8 ZJ $yr^{-1}$ to ~8.0–11.5 ZJ $yr^{-1}$ over the same time periods. This quantification of acceleration is valid for >15-year periods, but its detection can be hampered by short-term fluctuations in OHC. At interannual timescales, global OHC fluctuations are dominated by El Niño–Southern Oscillation (ENSO) events[79,80,83]. During and after El Niño events, OHC decreases as some heat makes its way into the atmosphere, contributing to a temporal global surface warming. Major volcanic eruptions have also caused interannual to decadal cooling phases (Agung in 1963, El Chichón in 1982 and Pinatubo in 1991)[84,85]. Nevertheless, a shorter time series of EEI also reported an increase in rates since the early 2000s[7,66,86], and the interplay between long-term change and interannual natural variations still needs to be elucidated.

A robust long-term acceleration is also evident in CMIP5 and CMIP6 simulations[85,87,88], highlighting the anthropogenic connection to this accelerated warming (FIG. 2b,d). Indeed, detection and attribution research indicates that observed multidecadal-scale changes in global OHC are primarily the result of anthropogenic GHG emissions (partly offset by anthropogenic aerosols and volcanic forcings)[85,89–91], and that they have already emerged from background natural internal climate variability[92,93]. The OHC rate increase since 2001 is also thought to be driven by a large decrease in reflected solar radiation with a small increase in emitted infrared radiation associated with anthropogenic forcing[94].

***Global deep and full-depth changes.*** Ocean warming is also evident at depth (FIG. 2e,f and TABLE 1). For instance, from 1958 to 2019, global OHC gain below 2,000 m is estimated at 26.0 ± 16.6 ZJ, or 0.43 ± 0.27 ZJ $yr^{-1}$. This estimate assumes that anthropogenic influence is not detectable before 1991 owing to the long response time of the deep ocean[38,58,59], but such deep layers might be affected by past climates that could offset a portion of the anthropogenic signal[95]. This post-1991 uptake assumption has an observational basis. For example, high-quality hydrographic survey data indicate notable ocean warming of 0.06 ± 0.03 W $m^{-2}$ (0.96 ± 0.48 ZJ $yr^{-1}$) since 1992 (REFS.[3,96]). These warming signals are confirmed by other direct and indirect estimates[97], albeit with variability in magnitude, including from machine-learning[63] and variational minimization[98] approaches (FIG. 2e,f). Before the 1990s, observational estimates of OHC changes are more inconsistent[63,69,70] (FIG. 2e). However, the CMIP6 multimodel mean suggests a continuous increase in the deep ocean warming rate since the 1950s (FIG. 2f), but with substantial uncertainty due to diffusivity parameters, feedbacks and aerosols[99].

OHC estimates at 0–2,000 m and below-2,000 m can be combined to yield total OHC changes at full depth. In doing so, it is estimated that ocean warming was 378.4 ± 64.5 ZJ from 1958 to 2019 (6.20 ± 0.98 ZJ $yr^{-1}$)

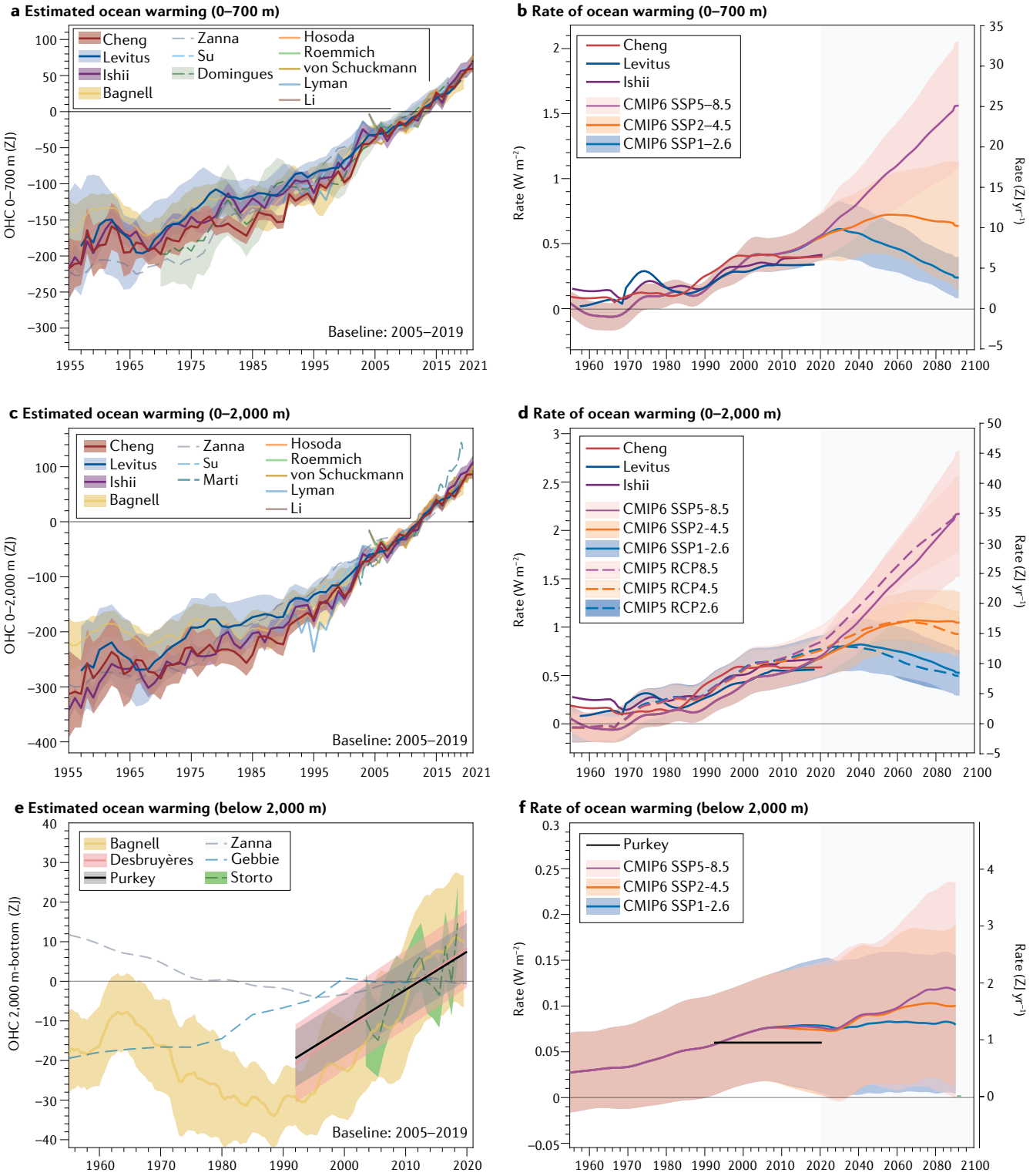


Fig. 2 | **Observed and projected ocean heat content changes. a** | Observed change in global annual 0–700-m ocean heat content (OHC) from 1955 to 2021, using various time series (listed by first author)[37,52,55,56,59,60,62–65,69,269]; Zanna represents the average of three estimates using different sea surface temperature datasets. Solid and dashed lines represent direct and indirect estimates, respectively, and shading indicates the 90% confidence intervals (±1.64$\sigma$). OHC anomalies are relative to a 2005–2019 baseline. **b** | Select observed (1955–2021) and modelled (1955–2100) rates of 0–700-m OHC change. Model time series are from CMIP6 and CMIP5 (for 0–2,000 m only), with bold lines depicting the ensemble means of historical simulations (1955–2014 for CMIP6 and 1955–2005 for CMIP5) and future projections under different scenarios (2021–2100) (Supplementary Table 3); shading represents the model spread (±1$\sigma$). Preindustrial control runs are used to adjust for simulation drift (Supplementary Information). **c** | As in **a** but for 0–2,000 m (REFS.[37,52,55,56,59,60,62,63,65,67,69,269]). **d** | As in **b** but for 0–2,000 m, and also including rates of change from CMIP5 (dashed lines). **e** | As in **a** but for below 2,000 m (REFS.[63,69,70,96–98]). **f** | As in **b** but for below 2,000 m. The ocean has been warming at an increasing rate since the 1950s, with warming irreversible this century.

Table 1 | **Total ocean heat content change and comparisons with previous assessments**

| Depth | OHC trend 1958–2019, this work[a,b] | OHC trend 1960–2018, GCOS[38] | OHC trend 1971–2018, this work[a,b] | OHC trend 1971–2018, IPCC-AR6[82] | OHC trend 1970–2017, IPCC-SROCC[6] | OHC trend 1971–2010, this work[a,b] | OHC trend 1971–2010, IPCC-AR5 (Box 3.1)[58] |
|---|---|---|---|---|---|---|---|
| 0–700 m | 229.5 ± 33.8 | 191.1 ± 10.7 | 203.9 ± 33.3 | 246.7 ± 80.6 | 208.8 ± 38.4 | 155.4 ± 29.7 | 172.8 ± 20.4 |
| | (0.23 ± 0.03) | (0.24 ± 0.03) | (0.27 ± 0.04) | (0.32 ± 0.10) | (0.27 ± 0.05) | (0.25 ± 0.05) | (0.27 ± 0.03) |
| 700–2,000 m | 121.9 ± 34.3 | 102.8 ± 7.9 | 103.9 ± 27.9 | 125.8 ± 27.8 | 108.0 ± 30.7 | 74.8 ± 22.6 | 57.2 |
| | (0.12 ± 0.04) | (0.13 ± 0.02) | (0.14 ± 0.04) | (0.16 ± 0.04) | (0.14 ± 0.04) | (0.12 ± 0.04) | (0.09) |
| 0–2,000 m | 351.4 ± 59.8 | 300.7 ± 19.4 | 307.9 ± 52.6 | 372.5 ± 85.3 | 316.8 ± 49.2 | 230.2 ± 47.0 | 230.1 |
| | (0.36 ± 0.06) | (0.35 ± 0.04) | (0.41 ± 0.07) | (0.48 ± 0.11) | (0.41 ± 0.06) | (0.37 ± 0.08) | (0.36) |
| 2,000–bottom | 26.0 ± 16.6 | 28.8 ± 12.2 | 26.0 ± 16.6 | 31.7 ± 15.8 | – | 18.3 ± 16.6 | 21.0 |
| | (0.03 ± 0.02) | (0.03 ± 0.01) | (0.03 ± 0.02) | (0.04 ± 0.02) | | (0.03 ± 0.03) | (0.04 ± 0.04) |
| Full depth | 378.4 ± 64.5 | 322.6 ± 30.8 | 333.8 ± 53.9 | 404.2 ± 112.3 | – | 248.5 ± 52.9 | 251.0 |
| | (0.39 ± 0.07) | (0.39 ± 0.04) | (0.44 ± 0.08) | (0.52 ± 0.15) | | (0.40 ± 0.08) | (0.39) |

Values are given in ZJ; values in parentheses are in W m$^{-2}$. GCOS, Global Climate Observing System; IPCC, Intergovernmental Panel on Climate Change; OHC, ocean heat content. [a]OHC estimates are based on three datasets[59,60,62], with trends calculated separately for each dataset based on locally weighted scatterplot smoothing (LOWESS)[81,259], and then averaged. Trends represent averages over the Earth's surface ($5.1 \times 10^{14}$ m$^2$). [b]90% confidence intervals are given, whereby uncertainty is quantified by estimating internal error and structural error separately, and assuming they are independent (see Supplementary Information). If instead it is assumed they are not independent, simply summing the two errors gives roughly 1.4 times larger error bars, as an upper limit.

and 333.8 ± 53.9 ZJ from 1971 to 2018 (7.10 ± 1.15 ZJ yr$^{-1}$), reinforcing evidence of OHC acceleration. These quantifications are broadly consistent with other direct and indirect results[5,38,59,63,69], but the estimate is ~17% smaller than IPCC-AR6 for the period of 1971–2018 (REF.[82]) (TABLE 1). Nevertheless, full-depth OHC estimates become more consistent after 1993 owing to increased data availability, totalling 245.7 ± 55.3 ZJ in this case and 263.0 ± 112.3 ZJ for IPCC-AR6 (REF.[82]) (Supplementary Table 2).

Thus, as a global average, OHC has increased dramatically at the surface, at depth, and over the entire water column. These changes are particularly evident after 1990 and are accelerating over time. However, these global estimates mask regional contrasts between ocean basins.

## Observed regional patterns of change

At the regional scale, there is distinct variability in surface and deeper OHC changes, with stronger area-averaged warming in the low- and middle-latitude Atlantic Ocean and southern oceans compared with other basins (FIG. 3). Here, OHC changes are assessed in six regions: the Pacific Ocean (35° S to 60° N), Atlantic Ocean (35° S to 64° N), Indian Ocean (35° S to 30° N), southern oceans (78°–35° S; the broad region south of Africa), the Mediterranean Sea and the Arctic Ocean. Given that the Cheng et al.[59] dataset minimizes regional errors through both mapping and instrumental bias correction[100–102], it is used to calculate these regional OHC changes for the upper 2,000 m (see Supplementary Fig. 1 for other datasets). Quantification of deep OHC below 2,000 m is limited by data availability and is thus not thoroughly discussed.

***Pacific Ocean.*** Changes in area-averaged Pacific Ocean OHC tend to resemble those of the global mean. Total OHC increased by 71.6 ± 8.2 ZJ from 1958 to 2019 for the upper 2,000 m (~20% of the global upper-2,000-m OHC increase), with an area-averaged change of 0.49 ± 0.06 × $10^9$ J m$^{-2}$ (FIG. 3c). This area-averaged change is comparatively smaller than other basins (FIG. 3a) owing to the large Pacific Ocean volume, and the less effective downward transfer of heat arising from an absence of deep water formation north of 35° S and limited mode water and intermediate water formation in the North Pacific[103].

In addition to these long-term area-averaged changes, there is pronounced spatial and temporal variability. Prior to 1990, a statistically insignificant trend of 0.05 ± 0.21 ZJ yr$^{-1}$ is observed, followed by a substantial OHC increase of 2.42 ± 0.29 ZJ yr$^{-1}$ since 1991 (FIG. 3c). Moreover, the Pacific Ocean warming pattern is characterized by weak and statistically insignificant trends in the western basin, and weak but robust warming (~0.25–0.5 W m$^{-2}$) in the east (FIG. 3a). Northeast Pacific regional warming is also significant and characterized by prolonged marine heat waves (MHWs) from 2014 to 2021 (REFS.[104,105]).

This spatial and temporal variability emerges due to the presence of strong modes of climate variability, particularly ENSO[79,106–108], the Interdecadal Pacific Oscillation (IPO) or Pacific Decadal Oscillation[109–111], and Atlantic Multidecadal Variability (AMV)[112,113]. For instance, in the tropical Pacific, OHC decreases by ~0.1–0.3 W m$^{-2}$ K$^{-1}$ during the transition from El Niño to La Niña. This change is linked to ocean heat release associated with anomalous warming of surface waters[79] and subsequent evaporative cooling, in turn causing warmer global-mean surface temperatures during El Niño years[114]. Besides, ENSO also causes regional OHC variability from month to month associated with an adiabatic redistribution of heat both laterally and vertically in the tropical ocean, resulting in a local monthly OHC change up to 100 W m$^{-2}$ K$^{-1}$ and an opposite OHC variation between 0–100-m and 100–300-m layers[79] (FIG. 3c).

Although interannual Pacific OHC fluctuations are primarily influenced by ENSO, decadal-scale changes are dominated by the IPO. During a negative phase, stronger trade winds and an enhanced shallow tropical

Mode water
Formed when winter mixed layers are convectively overturned owing to gravitational instability, and characterized by low potential vorticity and nearly vertically homogeneous temperature, salinity and density.

overturning increase OHU and subsurface heat storage[115]. This greater OHC increase is associated with a slowdown in global-mean surface air temperature increases[115,116]. The IPO, along with ENSO, also influences the ITF and thus heat redistribution between the Pacific and Indian Oceans[107,117]. Again during a negative IPO phase (or a La Niña event), model and observational evidence indicates that a substantial amount of heat can be transported from the Pacific to the Indian Ocean[107,118–120]. In the northwest Pacific, however, AMV governs decadal variability in North Pacific subtropical mode water and thereby OHC change[112,121]. For instance, during a positive AMV, as observed since ~1980, warming anomalies in the North Atlantic Ocean led to a poleward expansion of the westerly wind belt[114] and the subtropical ocean circulation[122,123], and a resulting large OHC anomaly in the northwest Pacific Ocean[112]. As a result of this decadal variability, OHC trends calculated over these timescales are influenced by the start and end points of the analysis, and are therefore somewhat uncertain.

***Atlantic Ocean.*** OHC changes in the Atlantic are larger than those observed in the Pacific (FIG. 3a,d). Indeed, in the upper 2,000 m, OHC increased by 117.2 ± 7.5 ZJ over 1958–2019 (~33% of the global upper-2,000-m OHC increase), with an area-averaged warming of $1.42 \pm 0.09 \times 10^9$ J m$^{-2}$, ~3 times that for the Pacific Ocean (FIG. 3c). Spatial and temporal variability is also evident. For example, the Atlantic OHC trend doubled from 1.29 ± 0.19 ZJ yr$^{-1}$ in 1958–1990 to 2.66 ± 0.27 ZJ yr$^{-1}$ in 1991–2019, indicating an earlier onset of warming in the Atlantic than the Pacific. The Atlantic is further host to some of the largest rates of regional OHC changes, >1 W m$^{-2}$ in most regions between about 35° S and 40° N, but exceeding 2 W m$^{-2}$ in the Gulf Stream of the North Atlantic (FIG. 3a).

Yet, whereas warming dominates the Atlantic average and regional signatures, cooling and a resultant reduction in heat content is evident at subpolar latitudes of the North Atlantic (~45–70° N, ~70° W to 0°) down to >800 m depth[124] (FIG. 3a). The mean rate of OHC change is −0.6 W m$^{-2}$ in this region since 1958. This 'cold blob' and the apparent cooling/warming dipole are a predicted consequence of circulation changes and heat redistribution in response to GHG and aerosol forcing[4,24,27,90,125,126]. Notably, these circulation responses include a slowdown of Atlantic Meridional Overturning Circulation (AMOC)[127,128], the fingerprint of which closely matches that of the OHC pattern[129,130]. However, there is a lack of long-term observational evidence for this AMOC slowdown, with some direct and indirect estimates suggesting a subtle reduction in meridional heat transport at 26° N in the Atlantic[128,131–133], in concert with fluctuations in the North Atlantic Oscillation[134] (NAO). Moreover, modelling results are inconsistent in terms of the spatial pattern and timing of the cold blob in response to AMOC changes[135,136], partly because of the incoherence of AMOC at different latitudes[137]. As such, changes in the AMOC and connections to the cold blob are still difficult to reconcile.

Atmospheric and air–sea interactions are vital processes in determining these North Atlantic OHC changes[138]. There have been substantial changes in the atmospheric circulation over the subpolar North Atlantic, including a northward movement of the jet stream and increased storminess[139,140]. Moreover, in the subarctic region where the cold blob is located, there is substantial heat loss attributable to intensified local winds associated with an NAO-like atmospheric circulation pattern during those winters[141,142]. A positive NAO favours strong westerly winds across the Atlantic mid-latitudes, bringing cooler drier air from North America and leading to increased winter surface heat and moisture fluxes into the atmosphere[143]. This elevated surface flux cools the ocean, increases deep water formation in the Labrador Sea area, and leads to a stronger AMOC several years later[143,144]. North Atlantic subpolar cooling has also been traced to the remote impact of Indian Ocean via atmospheric teleconnections[145].

***Indian Ocean.*** In the Indian Ocean, OHC changes have been more subdued until the late 1990s. Here, total upper-2,000-m warming is 32.1 ± 4.0 ZJ from 1958 to 2019 (accounting for ~9% of the global upper-2,000-m OHC increase), and area-averaged warming $0.70 \pm 0.08 \times 10^9$ J m$^{-2}$. Although the total Indian OHC increase is smaller than other basins because of its area, this area-averaged warming is slightly larger than the Pacific Ocean but much smaller than the Atlantic Ocean. Observational estimates suggest a statistically insignificant trend of −0.05 ± 0.10 ZJ yr$^{-1}$ from 1958 to 1990 (FIG. 3e), consistent across different datasets[146] (Supplementary Fig. 1). However, from the late 1990s, rapid warming is evident, reaching 1.21 ± 0.14 ZJ yr$^{-1}$ from 1991 to 2019, about half of the Pacific warming during the same period. The weak warming trend before 2000 has been attributed to interdecadal changes in the Indo-Pacific Walker circulation and a corresponding upper-layer cooling of the tropical Indian Ocean, moderating GHG-induced warming[147]. By contrast, the unprecedented rapid warming since 2000 has been linked to increased wind-driven heat transport in the ITF during the negative phase of the IPO[120,148]. Local wind and heat flux forcing also had a substantial contribution[146].

In addition to these decadal-scale fluctuations, there is also substantial year-to-year variability. For example, 12 ZJ of heat was lost from 2015 to 2018, with a similar magnitude of recovery from 2019 to 2020 (FIG. 3e). These pronounced interannual fluctuations in Indian Ocean heat content are partly controlled by ENSO via its atmospheric teleconnection to the Indian Ocean basin mode[149,150] and impacts on the ITF[106,117,151]. During the 2015/2016 super El Niño event, for example, an unprecedented reduction of ITF volume and heat transport was responsible for the sharp reduction of OHC in the Indian Ocean[107,119]. The Indian Ocean is also modulated by Southern Ocean variability and climate trends, including the observed poleward migration of westerly winds, a southward shift of the subtropical gyre and resulting multidecadal trends in regional OHC[152–154] over the subtropical southern Indian Ocean.

***Southern oceans.*** Significant warming trends have also been identified over the southern oceans[155–157], defined here as the entire region south of 35° S. Total warming in the upper 2,000 m is estimated at 126.6 ± 8.1 ZJ from

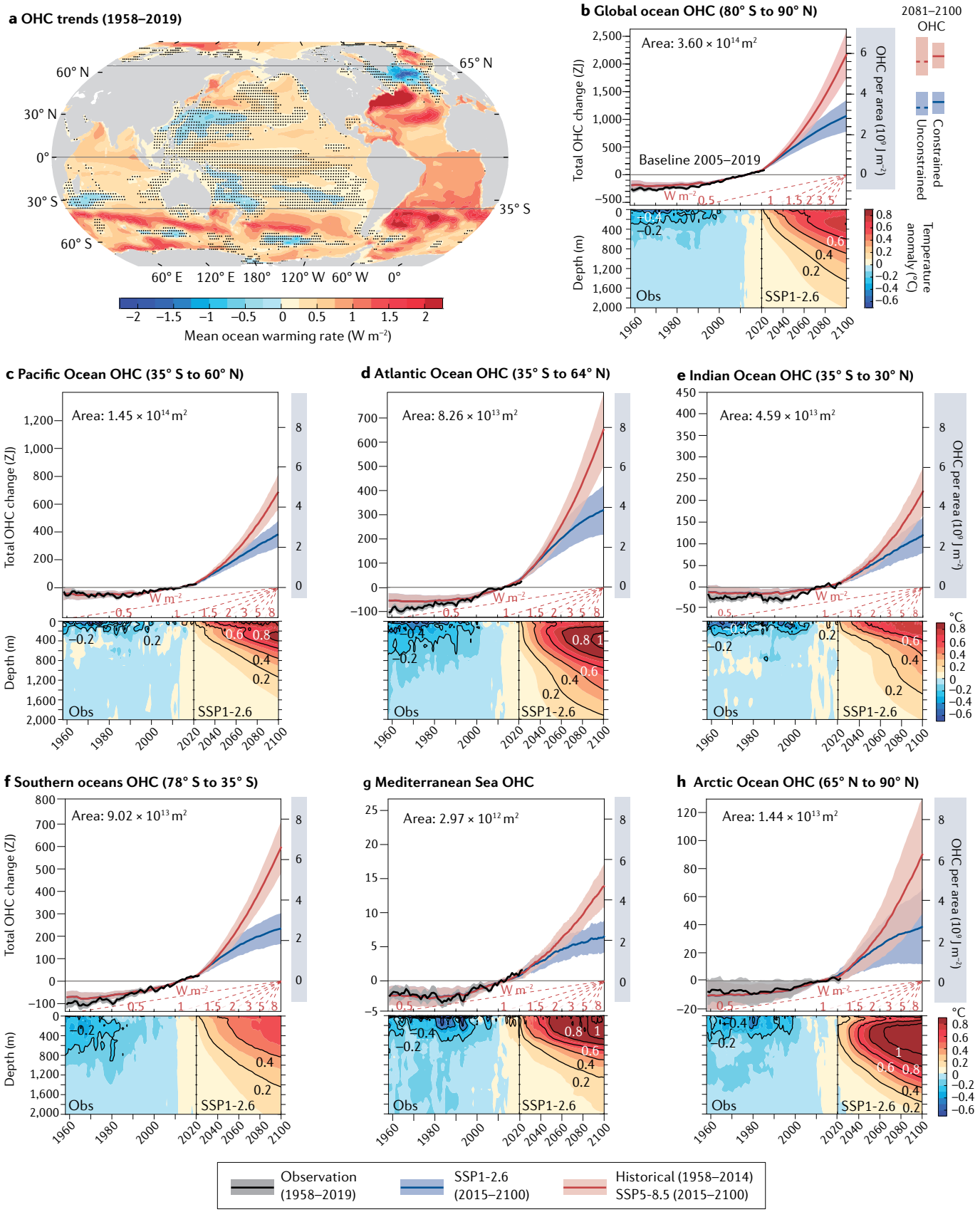


1958 to 2019 (accounting for ~36% of the global upper-2,000-m OHC increase), equating to $1.40 \pm 0.09 \times 10^9$ J m$^{-2}$ (FIG. 3f). The rate of southern oceans warming has almost doubled from $1.49 \pm 0.23$ ZJ yr$^{-1}$ over 1958–1990 to $2.72 \pm 0.29$ ZJ yr$^{-1}$ over 1991–2019, and is consistent across datasets (Supplementary Fig. 1). Hence the

Fig. 3 | **Observed and projected regional OHC changes. a** | Observed OHC trends from 1958 to 2019 (REF.[59]), with non-stippled regions depicting regions with statistically significant trends at the 90% confidence level. **b** | Total (left axis) and per-area (right axis) annual OHC changes from observations[59] (black), and CMIP6 ensemble means under shared socioeconomic pathways SSP1-2.6 (blue) and SSP5-8.5 (red), all relative to a 2005–2019 baseline. Constrained and unconstrained projections for 2081–2100 are provided in bars in **b**, and in all other places unconstrained results are presented. Shading depicts model spread of ±1$\sigma$. Red dashed lines illustrate the linear slope of the heating rate (for global, the Earth's surface is used; for each basin, its area is used). The lower panel depicts temperature anomalies as a function of depth and time from observations (1958–2019) and SSP1-2.6 (2020–2100), relative to a 2005–2019 baseline (see Supplementary Fig. 8 for SSP5-8.5 equivalents). **c** | As in **b**, but for the Pacific Ocean. **d** | As in **b**, but for the Atlantic Ocean. **e** | As in **b**, but for the Indian Ocean. **f** | As in **b**, but for the southern oceans. **g** | As in **b**, but for the Mediterranean Sea. **h** | As in **b**, but for the Arctic Ocean. Although present in all basins, ocean warming is unevenly distributed, with future warming dependent on socioeconomic scenarios.

southern oceans act as the largest heat reservoir since the 1950s, holding twice the excess anthropogenic heat as the Pacific. This OHC trend is broadly consistent with that of the Atlantic, which collectively reveal more intensive local warming than other basins.

In the southern oceans, these strongest regions of warming are concentrated on the northern flank of the main fronts of the Antarctic Circumpolar Current (ACC) (FIG. 3a) (note also distinct surface cooling north of the Ross Sea[158,159]). These long-term OHC changes are primarily attributable to greenhouse gas forcing, with a secondary role of stratospheric ozone depletion[160,161], via several processes. For example, wind-driven upwelling of unmodified deep water keeps surface ocean cold, and the cold water absorbs anthropogenic heat which is then exported to the northern flank of the ACC by the background overturning circulation. There, it is subducted in the deep mixed layers formed north of the ACC[162,163]. These deep mixed layers are associated with the formation of subantarctic mode water[164,165], and, in turn, Antarctic Intermediate Water — it is these waters that are absorbing significant quantities of anthropogenic heat[166]. However, model limitations along with sparse measurements have hampered understanding of the southern oceans' changing hydrography[167–169]. For example, theoretical predictions and high-resolution ocean modelling suggest that the observed strengthening of the westerly winds would drive an increase in eddy activity without changing the mean ACC transport, because the energy cascades rapidly into small-scale eddy fields[170–172]. This effect should, in turn, impact ocean interior mixing[173] and ocean heat content trends, but modern-day climate models do not generally resolve mesoscale eddies over the southern oceans.

Other processes are also thought to be important in driving OHC changes to the north of the ACC. For instance, lateral currents driven by buoyancy and steered by topography are associated with an observed acceleration of the zonal geostrophic currents within 45° S to 60° S. The change of currents leads to anomalous heat transport that relates to the pattern of OHC[174]. Moreover, freshening, linked to an amplification of the global hydrological cycle and sea-ice and ice-shelf changes, has weakened entrainment of subsurface warm water and could regulate warming patterns in the southern oceans[175,176]. Furthermore, the change in Antarctic sea-ice extent (a decrease since late 2016 after decades of increase) is probably associated with atmospheric circulation variations (the southern annular mode), and then could regulate the surface heat flux and OHC[13,177,178].

In addition, the Tasman Sea has also witnessed substantial OHC increases[179,180], particularly near southeastern Australia (FIG. 3a). Changes here are potentially linked to a southward migration of the East Australia Current extension[119] and a reduction in the ITF, linked to heat redistribution by variability in ocean circulation[125].

Abyssal ocean warming is consistent with a reduced volume of Antarctic Bottom Water entering the deepest ocean layers. This abyssal warming has been linked to a meltwater-induced slowdown of the lower cell of the global meridional overturning circulation[181], which would be consistent with abyssal OHC changes being largely due to heat redistribution, and not via anthropogenic heat uptake within the lower overturning cell.

***The Mediterranean Sea.*** In the Mediterranean Sea, upper-2,000-m OHC increased by 3.3 ± 0.4 ZJ from 1958 to 2019, with area-averaged warming of $1.11 \pm 0.12 \times 10^9$ J m$^{-2}$. This OHC increase exceeds the global, Pacific, Indian and Arctic Ocean changes (FIG. 3g). As in these other basins, warming trend is superimposed by multidecadal variability[182,183], with OHC rate increasing from −0.01 ± 0.01 ZJ yr$^{-1}$ for the period of 1958–1990 to 0.12 ± 0.01 ZJ yr$^{-1}$ after 1991.

The Mediterranean Sea is linked with the adjacent North Atlantic Ocean via their overturning circulation systems[184,185], which exert control over the basin's ocean heat budget in addition to the local surface heat flux[186,187]. In the upper ocean, the Atlantic water (0–150 m) flows into the Mediterranean Sea and moves eastward, so the climatic conditions along this path are crucial in determining the heat content. A stronger OHC increase in the eastern basin (where warmer intermediate waters formed) than the western basin is linked to the anomalous atmospheric conditions and reduced river freshwater input[124,188]. These warmer (and also saltier) intermediate waters then spread towards the western basin at sea subsurface (150–450 m) on their way back to the North Atlantic[189,190]. The increasing transport of heat from the eastern to the western Mediterranean affects the deep water formation process in the Gulf of Lion, enhancing the tendency of this site to produce warmer and saltier deep waters[188,191]. When the heat of the intermediate and deep waters flows out of the Strait of Gibraltar (Mediterranean Outflow Water), it, in turn, influences the meridional overturning circulation in the Atlantic Ocean[188,192,193].

***Arctic Ocean.*** The Arctic Ocean has been steadily warming. Total upper-2,000-m OHC increased by 8.6 ± 1.3 ZJ from 1958 to 2019, equating to area-averaged changes of $(0.59 \pm 0.09) \times 10^9$ J m$^{-2}$. Accordingly, about 2.5% of excess heat in the global upper-2,000-m ocean is stored in the Arctic basin since 1958 (3.3% since 1991)[124,194], much of it being in the Atlantic Water layer[20,194]. Most of this OHC increase has occurred since the 1990s[195] (FIG. 3h), with statistically significant warming rates of 0.29 ± 0.05 ZJ yr$^{-1}$ since 1991 compared with

$0.01 \pm 0.03\,ZJ\,yr^{-1}$ from 1958 to 1990. While statistically significant, uncertainty of the Arctic OHC time series is much larger than for the other five basins (FIG. 3h) owing to reduced subsurface data availability in sea-ice conditions. Nevertheless, observational datasets and a reanalysis product[194] exhibit consistent long-term changes for Arctic OHC (Supplementary Fig. 1).

OHC changes in the Arctic Ocean are strongly affected by rapid environmental changes, ocean heat transport and local air–sea/ice–sea heat exchanges[20,194]. For instance, ocean warming can be directly affected by heat transport into the region associated with the rapid decline of sea ice and the concurrent expansion of Atlantic waters into the Arctic Ocean ('Atlantification')[196–199]. However, direct observations reveal no significant trend in heat transport from the subtropical North Atlantic to the Arctic from 2014 to 2018[119,200], although others suggest an increase from 1993 to 2016[201], highlighting disparities related to both data uncertainty and substantial interannual variability[20]. Other environmental changes also affect Arctic Ocean OHC, including amplified surface warming since the 1960s at a rate twice the global value, driven by positive surface heat flux into the ocean associated with reduced outgoing longwave radiation and a reduction in albedo from the sea-ice–albedo feedback[23,197]. However, the air–sea/ice–sea heat exchanges are currently poorly quantified because of the data insufficiency[20].

Thus, over 1958–2019, the southern oceans and Atlantic Ocean are the main heat reservoir, accounting for 36% and 33% of the global OHS, respectively; the Pacific and Indian oceans account for the other 20% and 9%. However, the percentages change with time and ocean area, given strong decadal variability of OHC change in each basin. Area-averaged warming is larger in the southern oceans, Atlantic Ocean and Mediterranean Sea ($\sim 1.11–1.42 \times 10^9\,J\,m^{-2}$) compared with the other basins ($\sim 0.49–0.70 \times 10^9\,J\,m^{-2}$), indicating very intensive warming mainly associated with the ocean circulations.

## Ocean warming projections

In addition to the observed OHC changes, past GHG emissions have also committed the global ocean to future warming, the magnitude of which is dependent on the future socioeconomic pathway[6,202] (FIG. 3). Using drift-corrected models from the CMIP6 archive (Supplementary Table 3; Supplementary Fig. 2), these projected OHC changes are now discussed for the globally averaged ocean and for individual basins.

***Global change projections.*** The CMIP6 models project continued ocean warming as a result of past and future GHG emissions. Under shared socioeconomic pathway SSP5-8.5, a high-emission scenario, total upper-2,000-m warming is estimated at 1,769 ZJ [1,523–2,206 ZJ; the 17–83% error range around a central estimate] by the end of the century (2081–2100 average relative to 2005–2019). For SSP1-2.6, a low-emission scenario, this OHC change becomes 930 [798–1,227] ZJ (FIG. 3b). However, these projections are strongly influenced by individual models' equilibrium climate sensitivity (ECS). Specifically, some CMIP6 models exhibit ECS > 5 K (REF.[92]) (Supplementary Figs. 3–7), and those models with higher ECS tend to project stronger ocean warming by the end of the century owing to strong correlations between those metrics[203,204]. As such, there is strong motivation to use observational trends from 2005–2019 to better constrain future projections[205] and produce more realistic OHC estimates (Supplementary Information).

In doing so, global OHC trends are slightly enhanced and uncertainties reduced, with the weight of both very low and very high ECS models being reduced. Total observationally constrained upper-2,000-m warming by the end of the century is estimated at 1,030 [839–1,228] ZJ and 1,874 [1,637–2,109] ZJ for SSP1-2.6 and SSP5-8.5, respectively (FIG. 3b). These projections are broadly consistent with CMIP5 results[5,205] (FIG. 2d), and represent OHC changes ~2–4 and ~4–6 times the observed 1958–2019 value (TABLE 1 and Supplementary Table 4). Projections for 0–700 m and full depth are 1,221 [1,021–1,422] ZJ and 1,967 [1,721–2,205] ZJ for SSP5-8.5, 561 [408–723] ZJ and 1,103 [907–1,297] ZJ for SSP1-2.6 (Supplementary Table 4 and 5). Importantly, these observationally constrained projections result in a substantial reduction in the uncertainty range, especially the upper bound (Supplementary Table 4 and 5). Thus, the largest CMIP6 projections from both very low and very high ECS models are very unlikely as they overestimate ocean warming over 2005–2019.

In addition to differences in total OHC between scenarios, rates of warming also vary. For instance, the projections (here unconstrained) indicate that, in the upper 2,000 m, the ocean warming rate will probably peak between about 2030–2040 at ~0.8 $W\,m^{-2}$ and then decrease to ~0.5 $W\,m^{-2}$ at the end of this century for low-emission scenarios (SSP1-2.6 and RCP2.6; FIG. 2d). In contrast, for a high-emission future (SSP5-8.5 and RCP8.5), ocean warming continues to increase throughout the twenty-first century to ~2.0–2.2 $W\,m^{-2}$ by the 2090s, ~4 times the current level of OHU (FIG. 2d). Such scenario differences are also evident in the upper 700 m; OHC rates peak at ~0.5–0.6 $W\,m^{-2}$ around 2030 and decrease to ~0.2–0.3 $W\,m^{-2}$ during the 2090 s for SSP1-2.6, and continue increase to ~1.5 $W\,m^{-2}$ during the 2090s for SSP5-8.5 (FIG. 2b). At depth (<2,000 m), these scenario differences are much smaller (FIG. 2f).

The vertical structure of global ocean warming is further distinct under different scenarios. For SSP1-2.6, global sea surface warming is stabilized at ~0.6 °C (relative to a 2005–2019 baseline) after ~2050 (FIG. 3b), consistent with the Paris Agreement of limiting global surface temperature to 2 °C above the preindustrial level. However, subsurface (below ~100 m) warming continues, and anthropogenic heat penetrates the deep layers in all ocean basins (FIG. 3b). For SSP5-8.5, both global surface and subsurface warming continues to the end of this century and beyond, with a surface warming of >2.8 °C and upper-600-m warming of >1°C above the 2005–2019 average (Supplementary Fig. 8).

***Transient climate response and the vertical structure of OHC.*** The considerable heat penetration into the ocean interior critically affects surface temperature and therefore the global climate. The rate of OHC increase and

Shared socioeconomic pathway
The SSPs are a set of plausible trajectories of societal development and radiative forcing. SSP1-2.6 is a relatively low-emission scenario, representing the pathways to limit the global surface warming below 2 °C, which requires immediate, rapid and large-scale reductions in greenhouse gas emissions. SSP5-8.5 is a higher emissions scenario with projected warming >3 °C by 2100.

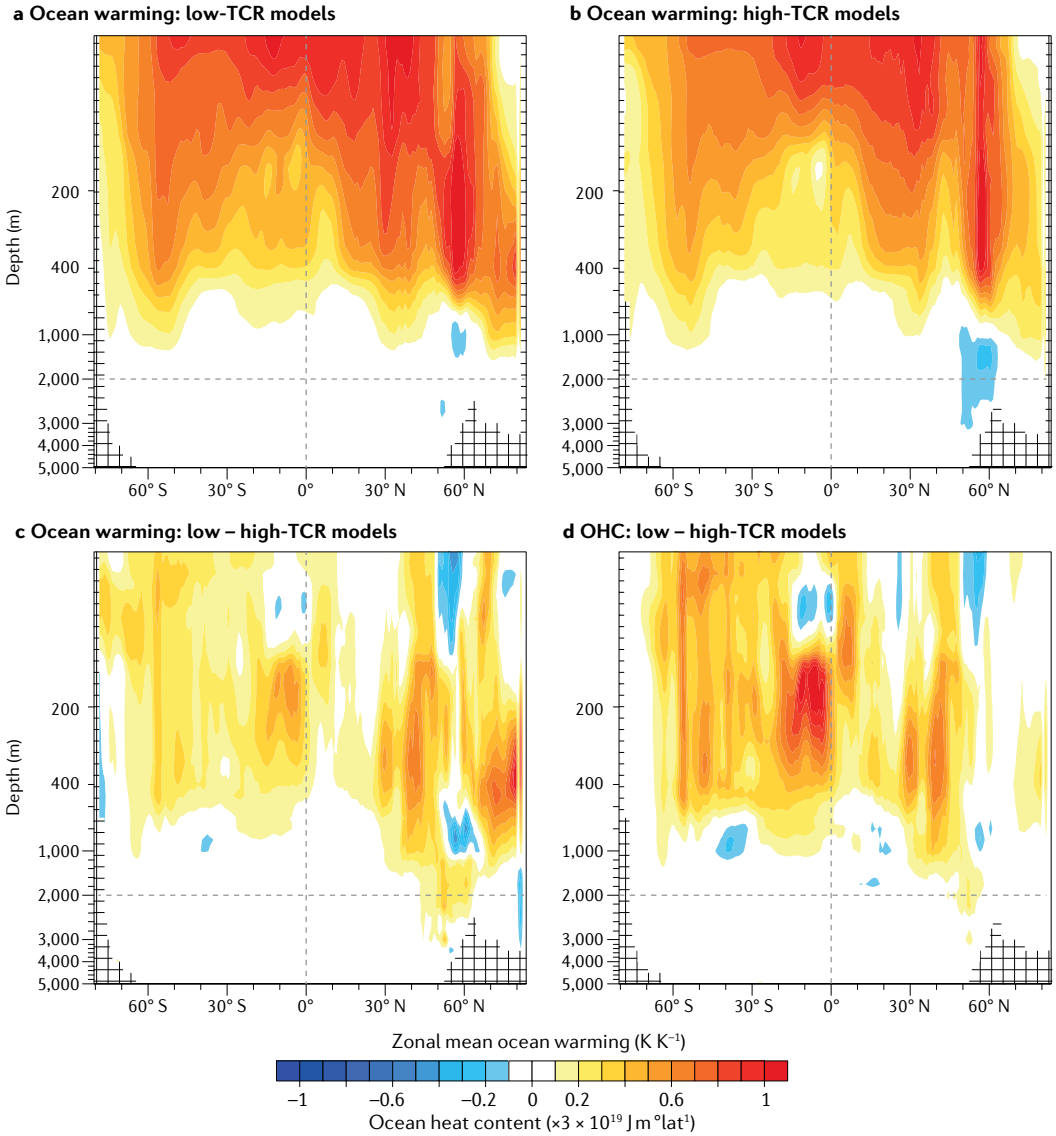


Fig. 4 | **Relationship between transient climate response and the vertical structure of temperature and OHC.** **a** | Zonal mean ocean warming with depth normalized by global-mean near-surface air temperature warming from years 1 to 70 of 1% $CO_2$ simulations from CMIP6 for five models with the lowest TCR. **b** | As in **a**, but the five CMIP6 models with the highest TCR. **c** | The difference between **a** and **b**. **d** | Associated differences in heat content change between the lowest- and highest-TCR models. Higher efficiency of ocean heat transport from the upper into the deeper ocean has a negative effect on the surface temperature increase for transient climate response.

the efficiency with which heat is transported from the upper ocean into the deeper ocean are critical in setting the strength and timescale of the climate adjustment in response to anthropogenic influences[24,203,206]. One important climate-change metric is the transient climate response (TCR), the surface warming under a 1% per year $CO_2$ increase from preindustrial values at the time of $CO_2$ doubling (70 years). The rate and patterns of ocean heat content are linked to TCR via the coupling at the sea surface[203,207].

Both low- and high-TCR models reveal strong warming from the Equator to 30° N, and warming to greater depths in higher-latitude ocean areas (FIG. 4a,b). However, in low-TCR models, there is a greater warming at depth compared with models with high TCR (FIG. 4c). These differences exist at all latitudes down to 1,000 m depths, although differences are weakest in regions of strong warming from the Equator to 30° N.

When integrated across the volumes of water for OHC (FIG. 4d), the Southern Hemisphere indicates stronger intermodel contrasts than the Northern Hemisphere. The strongest contrasts are found near the equatorial undercurrent, the origin of which remains an open question. The differences in the North Atlantic intermodel contrasts are likely to be due to the overturning circulation response to a warming climate. A key role for changes in upper-ocean salinity driven by both the surface freshwater flux and winds has been identified, with consequences for both the patterns and magnitudes of warming in coming decades[208,209]. Given the role of salinity and the fact that key cryosphere processes are absent from the current generation of climate

models used for future projections[210], important caveats exist regarding the ability to accurately estimate TCR and the latitudinal structure of future ocean warming. Nevertheless, the OHC differences between low- and high-TCR models reflect the higher OHU of low-TCR models (FIG. 4d).

***Regional trend projections.*** As discussed, the pattern of ocean warming has been non-uniform[4] (FIG. 3). Accordingly, although all six regional basins are expected to warm throughout the twenty-first century — exceeding 0.2 °C relative to a 2005–2019 baseline in the upper 1,200 m and at least 0.05 °C at 2,000 m — regional contrasts in rates of warming can be anticipated. These regional trends are now discussed, basing analyses on drift-corrected CMIP6 model projections without observational constraints, as the emergent constraint method only applies for global OHC change (FIG. 3c–h). Thus, regional biases in models have not been fully accounted for[211,212].

In the Pacific, total upper-2,000-m OHC change by the end of this century is projected to be 344 ± 74 ZJ for SSP1-2.6 and 575 ± 95 ZJ for SSP5-8.5 (FIG. 3c), ~3–6 times and ~6–10 times the observed changes over 1958–2019. Accordingly, the Pacific is expected to become the biggest heat reservoir owing to its large volume. However, the historical condition of low area-averaged warming continues. By the end of the century, area-averaged 0–2,000-m OHC reaches $2.37 \pm 0.51 \times 10^9$ J m$^{-2}$ and $3.97 \pm 0.66 \times 10^9$ J m$^{-2}$ for SSP1-2.6 and SSP5-8.5, respectively (FIG. 3c). By 2100, the 0.2 °C warming isotherm, a rough indicator of the vertical extension of warming, is projected to reach depths of ~1,200 m under SSP1-2.6. This depth is shallower than all other basins, likely because the Pacific Ocean is dominated by shallow tropical and subtropical overturning cells, and ventilation of thermocline water (~150–200 m) via subduction in the subtropical gyres[213]. However, as current climate models are not skilful at capturing ENSO[214,215] and IPO[124] variability, future projections remain uncertain[211,214].

Similar to its past changes, the Atlantic Ocean is projected to undergo substantial warming. Total upper-2,000-m OHC increases are estimated to be 299 ± 84 ZJ for SSP1-2.6 and 546 ± 122 ZJ for SSP5-8.5, ~1–4 and ~3–6 times the observed 1958–2019 change, respectively (FIG. 3d). This heat gain is broadly consistent with that of the Pacific, despite representing only 57% of its area. Accordingly, the Atlantic witnesses some of the largest area-averaged rates of warming at 0–2,000 m: $3.62 \pm 1.02 \times 10^9$ J m$^{-2}$ for SSP1-2.6 and $6.61 \pm 1.48 \times 10^9$ J m$^{-2}$ for SSP5-8.5 (FIG. 3d). Moreover, the 0.2 °C anomaly isotherm reaches ~2,000 m and maximum basin-mean subsurface warming exceeds ~1 °C at 200–600 m by the end of the century under SSP1-2.6 (~1.6–2.8°C under SSP5-8.5). These large changes have been attributed to a decline of aerosol impacts in future Atlantic changes, reinforcing the greenhouse effect[216,217].

In the Indian Ocean, total 0–2,000-m warming is projected to be 108 ± 34 ZJ and 183 ± 43 ZJ by 2100 for SSP1-2.6 and SSP5-8.5, respectively (FIG. 3e), ~2–5 times and ~4–7 times that observed over 1958–2019. The area-averaged changes resemble those of the Pacific, and are projected to be $2.35 \pm 0.73 \times 10^9$ J m$^{-2}$ for the low-emission scenario, and $3.99 \pm 0.95 \times 10^9$ J m$^{-2}$ for the high-emission scenario (FIG. 3e). However, the uncertainty range is larger than projected for the Pacific, partly associated with substantial natural variability, and consistent with a large mismatch between observed and simulated Indian Ocean warming from 1958 to 2019. By 2100, the 0.2 °C warming isotherm reaches depths of ~1,500 m, deeper than the Pacific Ocean but shallower than the Atlantic Ocean (FIG. 3e).

As in the Atlantic, projected changes in the southern oceans are also large. Net upper-2,000-m warming is projected to reach 220 ± 60 ZJ for SSP1-2.6 and 505 ± 95 ZJ for SSP5-8.5 (FIG. 3f), ~1–3 times and ~3–5 times the 1958–2019 change, respectively. These net increases equate to area-averaged changes of $2.44 \pm 0.67 \times 10^9$ J m$^{-2}$ and $5.60 \pm 1.05 \times 10^9$ J m$^{-2}$, stronger than the Pacific and Indian Oceans, but increasingly smaller than the Atlantic Ocean, contrasting with observed changes. This large ocean warming is linked to accelerating subpolar westerlies and significant overturning of surface heat due to the formation of subantarctic mode water[164,165], Antarctic intermediate water[218] in the subpolar ocean, and Antarctic Bottom Water around the Antarctic continental margin[219], enhancing OHU and accumulation of heat just north of the ACC[163,216,220]. These water mass formations and vertical heat transports are reflected in deep-reaching warming by 2100, with the 0.2 °C anomaly isotherm expected to extend below 1,400 m (FIG. 3f). The uptake and drawdown of heat to depth is expected to slow around the Antarctic margin as meltwater and warming stratifies the surface mixed layer in those regions[181] and slows the formation of dense shelf water, but warming is expected to continue over much of the southern oceans.

The Mediterranean OHC increase at 0–2,000 m is expected to reach 6 ± 2 ZJ and 12 ± 2 ZJ for SSP1-2.6 and SSP5-8.5, respectively[221]. These changes are ~1–3 times and ~2–5 times observed values over 1958–2019, and reflect area-averaged changes of $2.06 \pm 0.60 \times 10^9$ J m$^{-2}$ and $4.09 \pm 0.72 \times 10^9$ J m$^{-2}$ (FIG. 3g). The 0.2 °C warming anomaly is projected to extend to ~1,200 m, which is deeper than for the global ocean[182] (FIG. 3g), owing to the thermohaline circulation in the Mediterranean Sea and efficient heat propagation to deeper layers[222,223]. Finally, in the Arctic Ocean, upper-2,000-m warming by 2100 is projected to reach 36 ± 22 ZJ for SSP1-2.6 and 76 ± 35 ZJ for SSP5-8.5 (FIG. 3h). These changes correspond to surface warming ~1–7 times and ~4–13 times that observed, totalling $2.50 \pm 1.54 \times 10^9$ J m$^{-2}$ and $5.25 \pm 2.45 \times 10^9$ J m$^{-2}$ for the low and high scenarios, respectively. Moreover, the 0.2 °C additional heat isotherm extends to ~1,800 m by the end of the century, and the >1 °C additional warming to within 100–800 m, spanning a larger depth than the Atlantic (FIG. 3h). The subsurface warming in the Arctic Ocean is much stronger than the global mean[224] (FIG. 3b,h). However, both the observational record and future warming in the Arctic are less reliable, given poor data coverage at the subsurface and the biases in Arctic Ocean hydrography and ice simulation in CMIP6 models[224].

***Drivers of future OHC patterns.*** The patterns of ocean warming are driven by the heat uptake at the ocean surface and the transport by currents, mixing and stirring in

the ocean interior. The patterns of ocean warming can be thought of as the sum of the added heat from the warming pattern set by surface heat fluxes and by the unperturbed ocean circulation (analogous to the uptake and transport of passive tracers), and the redistributed heat as the transport of the OHU by the perturbed circulation[27,127]. These added and redistributed contributions to the total regional heat content changes can be quantified using a subset of models with carbon cycle[27] (FIG. 5).

Over the historical period (here, 1958–2015), the total heat patterns are dominated by the redistribution, with a pattern correlation between total and redistributed heat of $R = 0.84$ on average (FIG. 5d,j and Supplementary Fig. 9). Indeed, warming along the Kuroshio extension, the southern oceans and to some extent the high-latitude North Atlantic are associated with redistribution of the pre-1958 temperatures from the changing ocean circulation in these regions, in broad agreement with observational inferences during 2000–2015 (REFS.[125,225]). Note, however, that the redistribution pattern varies widely across CMIP models. In contrast, warming in the subtropical Atlantic basin, which has emerged over the

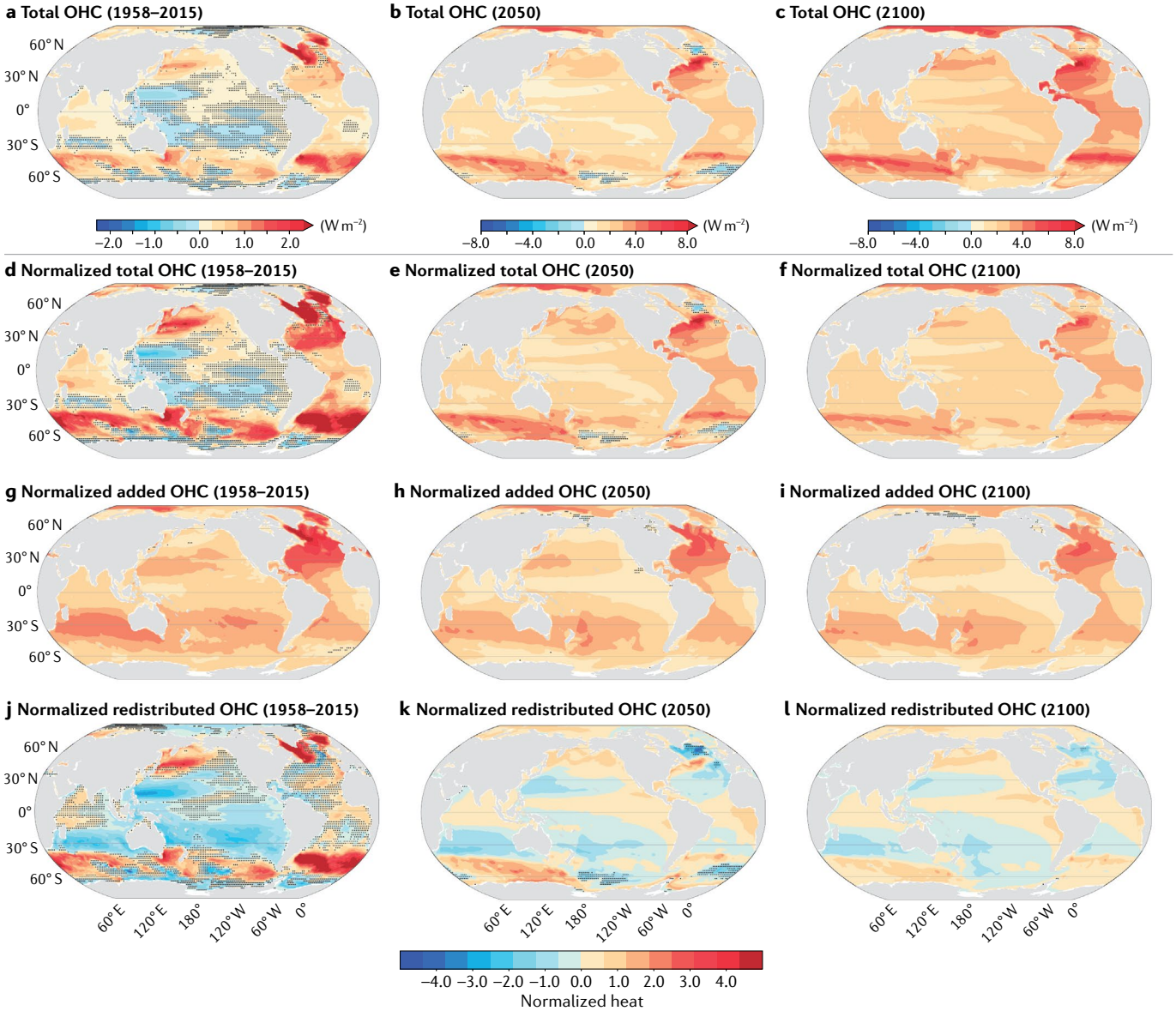


Fig. 5 | **Simulated past and projected future ocean heat content change.** **a** | Total OHC changes over 1858–2015 from an ensemble of 11 CMIP6 models. **b** | Total OHC changes centred on 2050 (the 5-year mean from 2048–2052), relative to the 2015–2020 mean, from an ensemble of 7 CMIP6 models. **c** | As in **b**, but centred on 2100, representing the 5-year mean from 2095 to 2100. **d** | As in **a**, but normalized by global ocean heat uptake. **e** | As in **b**, but normalized by global ocean heat uptake. **f** | As in **c**, but normalized by global ocean heat uptake. **g** | As in **a**, but for added OHC normalized by global ocean heat uptake. **h** | as in **b**, but for added OHC normalized by global ocean heat uptake. **i** | As in **c**, but for added OHC normalized by global ocean heat uptake. **j** | As in **a**, but for redistributed OHC normalized by global ocean heat uptake. **k** | As in **b**, but for redistributed OHC normalized by global ocean heat uptake. **l** | as in **c**, but for redistributed OHC normalized by global ocean heat uptake. Stippling indicates where the multimodel mean anomaly is less than the intermodel standard deviation. See Supplementary Information for list of models used. The patterns of ocean warming are mainly driven by the redistributed heat as the transport of the OHU by the perturbed circulation in the historical era, but are projected to be dominated by added heat in the twenty-first century, set by surface heat fluxes and the unperturbed ocean circulation.

cooling effect of redistribution, is primarily associated with added heat in the CMIP6 ensemble (FIG. 5g).

Between 2015 and 2050, under SSP5-8.5 forcing, a warming signal is expected to emerge in most regions of the ocean (FIG. 5b,e and Supplementary Figs. 10 and 11). This overall warming pattern is primarily set by the passive uptake of added heat, with pattern correlations between total and added heat being 0.67 (FIG. 5e,h). The added heat pattern is likely to be dominated by warming within the subtropical gyres in all basins, on the equatorward flank of the ACC due to Ekman transport[156,163,226], and in the North Atlantic between ~30° N and 55° N due to heat uptake at high latitudes and southward transport at depth by the overturning circulation[69,227]. Exceptions to this overall warming pattern are evident in the North Atlantic warming hole and parts of the southern oceans, where cooling prevails (FIG. 5e). Trends in both these regions continue to exhibit a large spread across CMIP6 models and are dominated by redistribution patterns (FIG. 5k). Moreover, some of the added warming is partially offset by redistribution within the subtropics (~10°–30° N/S), consistent with CMIP5[27].

By 2100, all regions of the ocean are projected to exhibit warming under SSP5-8.5 (FIG. 5c,f and Supplementary Figs. 10, 11). At this time, the southern oceans and the Atlantic basin, along with most other regions, are heavily influenced by added heat (FIG. 5i). However, the redistribution of heat and circulation changes reduce net warming in the lower-latitude subtropics between ~10° and 30° N/S, and enhance warming in sectors of the mid-latitudes (between ~40° and 50° N/S) and along the equator (between ~10° S and 10° N) (FIG. 5l). This redistribution at 2100 is broadly consistent with the regional effects projected to emerge by 2050, with correlation patterns of 2050 and 2100 redistribution being 0.82. Idealized forcing experiments (flux perturbations under the flux-anomaly-forced model intercomparison project protocol[228–230]; 1% $yr^{-1}$ in CMIP5[231]), also reinforce this finding. Pattern correlations between 2050 and 2100 OHU (FIG. 5e,f), added heat (FIG. 5h,i) and redistribution (FIG. 5k,l), are also high, at >0.8, >0.85 and >0.75, respectively, indicating that future OHC patterns have already emerged by 2050.

Thus, ocean heat redistribution, although dominant in the past, becomes less important in the future (at least by 2050). Future patterns become more dominated by added heat associated surface heat flux and mean ocean circulation. As such, future ocean warming patterns might become more predictable in the coming decades[27]. However, further work is necessary to assess these results in high-resolution eddy-rich models.

## Impacts and consequences of ocean warming

Observed and projected ocean warming has substantial impacts across major Earth system components and scales (FIG. 1). For example, ocean warming accounts for more than 1/3 of global-mean sea level rise through thermal expansion, and thus dominates regional sea level patterns[82,202]. Sea level rise, in turn, increases the risks for coastal infrastructures and coastal habitats from salt water intrusion, coastal erosion and flooding in low-lying regions[232,233] (FIG. 1b). Ocean warming also decreases ocean density and increases upper-ocean stratification by 5.3% since 1960 (REF.[234]) (FIG. 1b), affecting the vertical and lateral exchanges of heat, carbon, oxygen, nutrients and other substances. The stratification increase, solubility reduction and circulation changes drive deoxygenation in the ocean interior by ~0.5–3.3% since the 1960s (REFS.[6,235]). By changing sea water buoyancy, ocean warming impacts ocean currents, for example, accelerating the zonally averaged Southern Ocean zonal flow in the upper layer[174]. Warmer water also reduces the efficiency of oceanic carbon uptake and storage[28,236] (FIG. 1b). The compounded effect of each of these impacts, especially following extreme events[236–238], poses more substantial stress on the environment than their individual effects[236] (FIG. 1b), driving, for example, changes in net primary and export production[239,240] with socioeconomic impacts on marine fisheries and aquaculture systems[241,242]. Indeed, it is projected that, driven by multiple stressors, the maximum catch potential of tropical fish stocks in some tropical exclusive economic zones will decline by up to 40% by the 2050s under the RCP8.5[242].

MHWs offer a strong example, whereby the relentless increase in OHC has direct implications for the frequency, intensity and extent of MHWs and other 'hot spots' within the ocean (FIG. 1b). With human-induced global warming and higher ocean heat content, it is inevitable that MHWs become more abundant, extensive and longer-lasting[237]. The highly anomalous ocean waters, including SSTs and upper OHC, often persist for more than a month[243], resulting in large impacts on ocean ecosystems and marine life. Effects from thermal stress causes mass mortality of benthic communities, including coral bleaching, changes in phytoplankton blooms, adverse effects on kelp forests and sea grasses, toxic algal blooms, shifts in species composition and geographical distribution, and decline in fish and fisheries and seabirds[105,238]. As such, MHWs modify ecosystem assemblages, biodiversity, population extinctions and redistribution of habitat[244,245].

One example is the prolonged MHW known as 'the blob' in the northeast Pacific and Gulf of Alaska from 2014–2016. This event greatly affected the ocean food web, shrinking phytoplankton blooms, which, in turn, diminished copepods, zooplankton and krill, and small fish, leading to the demise of ~1 million birds (notably murres), ~100 million cod and hundreds of humpback whales[104,105]. A similar unprecedented MHW in the south Tasman Sea in 2015–2016, where SSTs were up to 2.9 °C above normal owing to an ENSO-related alteration of the ITF and East Australian Current[119], also had substantial impacts[246]. Ecosystem impacts ranged from new disease outbreaks in farmed shellfish (oysters, abalone) and salmon, to mass mortality of wild mollusks, and many out-of-range observations of several fish species. Thus, with continued warming, MHW events and their impacts are expected to worsen: climate models project that the frequency of MHW might increase 50 times by 2081–2100 relative to 1850–1900 under RCP8.5 (REF.[247]).

Ocean warming also intensifies tropical cyclones[248], and associated changing ocean surface currents can indirectly affect pathways of storms[139] (FIG. 1b). In August 2017, the Gulf of Mexico became the warmest on record

to that point in the summertime. There was a strong link between upper OHC and record high rainfalls of over 60 inches (1,520 mm) over five days and extensive flooding in hurricane Harvey over parts of Texas[249]. Other processes at the air–sea interface affected by ocean warming include an increase of surface evaporation and rainfall[12,13], and an increase in precipitation anomalies tied to ENSO, and associated extreme weather events[250,251] (FIG. 1b).

Implications of ocean warming are also widespread across the Earth's cryosphere[195], and have in turn affected the ocean itself[252] (FIG. 1b). Examples include the thinning of floating ice shelves and marine terminating glaciers from basal ice melt[21,253], and the retreat and speedup of ice-sheet outlet glaciers in Greenland and Antarctica[254] and of tidewater glaciers in South America and in the Arctic[255].

Other particular concerns are the potential abrupt changes associated with warming, such as ocean circulation (for example, AMOC)[256] and ocean ecosystems[6,248]. Ocean warming is a key driving element for AMOC changes. The potential for abrupt AMOC collapse as a 'low-probability, high-impact' event cannot be ruled out in the future[6,247]. Each species of marine organisms has an optimal temperature window for functioning; most organisms are therefore vulnerable to warming[257]. It is projected that most tropical coral reefs will be threatened[258].

## Summary and future perspectives

In summary, OHC has changed substantially since the 1950s and is projected to continue to do so in the future. In the upper 2,000 m, net global increases of 351.4 ± 59.8 ZJ (0.36 ± 0.06 W $m^{-2}$) have been observed from 1958 to 2019, with the rate of warming accelerating from ~0.0–0.3 W $m^{-2}$ in the 1960s to ~0.5–0.7 W $m^{-2}$ in the 2010s. The pattern of ocean warming has been non-uniform in this historical era, including strong warming in the Atlantic and southern oceans, and overall is dominated by the redistribution of ocean heat by currents. Relative to 2005–2019, future warming is projected to reach 1,030 [839–1,228] ZJ for SSP1-2.6 and 1,874 [1,637–2,109] ZJ for SSP5-8.5 at the end of this century, ~2–4 (SSP1-2.6) to ~4–6 times (SSP5-8.5) the observed 1958–2019 change. On these timescales, added heat has an important role for OHC projections. Moreover, low GHG emissions would be likely to lead to a detectable and lasting reduction in ocean warming rate, with noticeable reductions in climate-change impacts. Indeed, given that ocean warming has already led to pervasive impacts and consequences, monitoring, understanding, adapting to and mitigating ocean warming must continue to be a high priority. Nonetheless, several gaps remain in measuring, estimating and understanding ocean warming.

First, the current ocean observing system needs to be sustained and extended to monitor OHC change at various spatiotemporal scales. The critical question of 'how adequate is the ocean observing system for monitoring the OHC changes at various timescales?' is still not fully answered. The international community have cast their eyes toward the future to improve not only the Argo fleet but also other measurement methodologies[259–261]. The ongoing and planned efforts include the maintenance of the current GOOS, and shipboard in situ measurements for calibration, validation and quality control of the Argo array; a drive toward spatial completion, including polar sea-ice zones, marginal seas and complicated channels; increased resolution in critical areas such as boundary currents and coastal areas; incorporation of deeper measurements (for example below 2,000 m); and inclusion of biological and chemical signals, along with temperature and salinity (Deep Argo and BioGeoChemical Argo programmes). The scientific community and funding agencies will need to be mindful of ensuring a continuous and comprehensive measurement network for the world's ocean — a network that incorporates new technologies as they are developed and retires old technologies that have outlived their usefulness, but with a good understanding of the handoff between technologies.

Second, uncertainty for OHC estimate needs to be better understood and quantified. In addition to data coverage, uncertainty also stems from mapping methods associated with data sampling, instrumental bias correction, choice of climatology, quality-control and other data processing procedures. These error sources are not independent of each other and are likely to lead to biases in current analyses. Thus, uncertainty in OHC estimate is method-dependent and producer-dependent. The contribution of each error source to the total OHC uncertainty is not fully understood, and the error range given by different datasets results in roughly 10-fold differences[33]. New approaches can be used to better quantify the uncertainty: for example, synthetic data for understanding and evaluating the mapping method, and exploiting ensembles (applying different techniques and forming an ensemble of OHC estimates)[59,262–264].

Third, syntheses of multisource (direct and indirect) observations and models are recommended to improve OHC estimates and mechanistic understanding. Synthesis of in situ observations with satellite-based observations (sea level altimetry, ocean colour, surface wind stress) and full atmospheric analyses shows the most promise. The indirect datasets can either serve as a cross-evaluation tool or constrain direct estimates, such as closing energy, water and sea level budgets. Attempts show promising results. As a coupled system, the separate impacts of atmospheric, ocean and ice (and other components) dynamics cannot be easily isolated[265], and identifying the coupling mechanism driving OHC patterns remains a high research priority. Capabilities for integrating different sources of Earth system observations and information (for example, model-based data assimilation and simulations) for a comprehensive quantification of the energy budgets should be built. For example, the integration of atmospheric and oceanic data leads to a quantification of MHT time series at all latitudes, capable of resolving interannual variability[133].

Fourth, the current generation of climate and Earth system models still contain non-negligible uncertainties in representing past and future ocean warming trends[202,205,212]. For example, there is substantial uncertainty in CMIP6 future projections in the Antarctic margin region, due to biases in simulated stratification[158], hydrography around the Antarctic shelf[266], and missing processes, including eddies, tides, ice-shelf cavities, and ocean–ice-shelf interactions. In the tropics, it is known

that tropical cyclones mix the ocean through substantial depths. Moreover, they form in hot spots and cool the ocean, yet they are largely absent from global models. In addition, interannual to decadal variability such as ENSO and the IPO remains poorly represented in modern-day climate models, yet they strongly control the pattern and timing of OHC anomalies. As ocean and atmospheric circulation have a key role in shaping the climate response (including ocean warming pattern and OHU efficiency)[127,203], evaluating the accuracy of the wind, atmosphere and ocean circulation projections should continue to be a research priority. A continuous process-based understanding of model performance is recommended including the understanding and identification of persistent biases in simulations, especially with respect to the diagnostics for Earth's major system cycles.

Fifth, understanding of extreme OHC events, their compound effects and past changes in OHC should be strengthened. For example, MHWs have been identified from surface conditions, but subsurface components are also important, and OHC as an indicator offers a way to integrate these aspects. The simultaneous occurrence of ocean warming extremes with other extremes (deoxygenation, acidification) requires special attention[236]. A more complete understanding of OHC changes in the deep past before the widespread availability of instrumental records is also critical to put the current changes in the context of a longer timescale[267]. Research on past climate change also helps us to understand how natural drivers and human influence have changed the Earth's climate system. The difficulty is a lack of full-depth temperature proxy data. Several methods have been developed to derive OHC change back to the past 20,000 years (Last Glacial Maximum), but the uncertainty is large[95,268].

## Data availability

The observation and model data used in this review are available at http://www.ocean.iap.ac.cn/. CMIP6 model data is available at https://esgf-node.llnl.gov/search/cmip6/.

Published online 18 October 2022


1. Hansen, J., Sato, M., Kharecha, P. & von Schuckmann, K. Earth's energy imbalance and implications. *Atmos. Chem. Phys.* **11**, 13421–13449 (2011).
2. Trenberth, K. E., Fasullo, J. T. & Kiehl, J. Earth's global energy budget. *Bull. Am. Meteorol. Soc.* **90**, 311–324 (2009).
3. Johnson, G. C. et al. Ocean heat content. *State of the Climate in 2020*, Global Oceans. *Bull. Am. Meteorol. Soc.* **102**, S156–S159 (2021).
4. Cheng, L. et al. Another record: ocean warming continues through 2021 despite La Niña conditions. *Adv. Atmos. Sci.* **39**, 373–385 (2022).
5. Cheng, L., Abraham, J., Hausfather, Z. & Trenberth, K. E. How fast are the oceans warming? *Science* **363**, 128–129 (2019).
6. Bindoff, N. L. et al. in *Special Report on the Ocean and Cryosphere in a Changing Climate* (eds Pörtner, H.-O. et al.) 477–587 (IPCC, Cambridge Univ. Press, 2019).
7. Loeb, N. G. et al. Satellite and ocean data reveal marked increase in Earth's heating rate. *Geophys. Res. Lett.* **48**, e2021GL093047 (2021).
8. Johnson, G. C. & Lyman, J. M. Warming trends increasingly dominate global ocean. *Nat. Clim. Change* **10**, 757–761 (2020).
9. Solomon, S., Plattner, G.-K., Knutti, R. & Friedlingstein, P. Irreversible climate change due to carbon dioxide emissions. *Proc. Natl Acad. Sci. USA* **106**, 1704–1709 (2009).
10. Abraham, J., Cheng, L., Mann, M. E., Trenberth, K. & von Schuckmann, K. The ocean response to climate change guides both adaptation and mitigation efforts. *Atmos. Ocean. Sci. Lett.* **15**, 100221 (2022).
11. Abram, N. et al. in *Special Report on the Ocean and Cryosphere in a Changing Climate* (eds Pörtner, H.-O. et al.) 73–129 (IPCC, Cambridge Univ. Press, 2019).
12. Cronin, M. F. et al. Air–sea fluxes with a focus on heat and momentum. *Front. Mar. Sci.* **6**, 430 (2019).
13. Trenberth, K. E. *The Changing Flow of Energy Through the Climate System* (Cambridge Univ. Press, 2022).
14. Yu, L. Global air-sea fluxes of heat, fresh water, and momentum: energy budget closure and unanswered questions. *Annu. Rev. Mar. Sci.* **11**, 227–248 (2019).
15. Held, I. M. & Soden, B. J. Robust responses of the hydrological cycle to global warming. *J. Clim.* **19**, 5686–5699 (2006).
16. Durack, P. J., Wijffels, S. E. & Matear, R. J. Ocean salinities reveal strong global water cycle intensification during 1950 to 2000. *Science* **336**, 455–458 (2012).
17. Liu et al. Enhanced hydrological cycle increases ocean heat uptake and moderates transient climate change. *Nat. Clim. Change* **11**, 848-853 (2021).
18. Wild, M. Global dimming and brightening: a review. *Geophys. Res. Lett.* **114**, D00D16 (2009).
19. Goode, P. R. et al. Earth's albedo 1998–2017 as measured from earthshine. *Geophys. Res. Lett.* **48**, e2021GL094888 (2021).
20. Mayer, M. et al. An improved estimate of the coupled arctic energy budget. *J. Clim.* **32**, 7915–7934 (2019).
21. Rintoul, S. R. et al. Ocean heat drives rapid basal melt of the Totten ice shelf. *Sci. Adv.* **2**, e1601610 (2016).
22. Wilson, N., Straneo, F. & Heimbach, P. Satellite-derived submarine melt rates and mass balance (2011–2015) for Greenland's largest remaining ice tongues. *Cryosphere* **11**, 2773–2782 (2017).
23. Timmermans, M.-L., Toole, J. & Krishfield, R. Warming of the interior Arctic Ocean linked to sea ice losses at the basin margins. *Sci. Adv.* **4**, eaat6773 (2018).
24. Winton, M., Griffies, S. M., Samuels, B. L., Sarmiento, J. L. & Frölicher, T. L. Connecting changing ocean circulation with changing climate. *J. Clim.* **26**, 2268–2278 (2013).
25. Exarchou, E., Kuhlbrodt, T., Gregory, J. M. & Smith, R. S. Ocean heat uptake processes: a model intercomparison. *J. Clim.* **28**, 887–908 (2015).
26. Whalen, C. B. et al. Internal wave-driven mixing: governing processes and consequences for climate. *Nat. Rev. Earth Environ.* **1**, 606–621 (2020).
27. Bronselaer, B. & Zanna, L. Heat and carbon coupling reveals ocean warming due to circulation changes. *Nature* **584**, 227–233 (2020).
28. Resplandy, L. et al. Quantification of ocean heat uptake from changes in atmospheric $O_2$ and $CO_2$ composition. *Sci. Rep.* **9**, 20244 (2019).
29. Gruber, N. Warming up, turning sour, losing breath: ocean biogeochemistry under global change. *Phil. Trans. R. Soc. A* **369**, 1980–1996 (2011).
30. Frölicher, T. L., Winton, M. & Sarmiento, J. L. Continued global warming after $CO_2$ emissions stoppage. *Nat. Clim. Change* **4**, 40–44 (2013).
31. Moltmann, T. et al. A global ocean observing system (GOOS), delivered through enhanced collaboration across regions, communities, and new technologies. *Front. Mar. Sci.* https://doi.org/10.3389/fmars.2019.00291 (2019).
32. Abraham, J. P. et al. A review of global ocean temperature observations: implications for ocean heat content estimates and climate change. *Rev. Geophys.* **51**, 450–483 (2013).
33. Meyssignac, B. et al. Measuring global ocean heat content to estimate the Earth energy imbalance. *Front. Mar. Sci.* https://doi.org/10.3389/fmars.2019.00432 (2019).
34. *Argo float data and metadata from global data assembly centre* (Argo GDAC, 2000); https://doi.org/10.17882/42182.
35. Riser, S. C. et al. Fifteen years of ocean observations with the global Argo array. *Nat. Clim. Change* **6**, 145–153 (2016).
36. Boyer, T. P. et al. *World Ocean Database 2018*. NOAA Atlas NESDIS 87 (technical ed. Mishonov, A. V.) (NOAA, 2018).
37. von Schuckmann, K. et al. Consistency of the current global ocean observing systems from an Argo perspective. *Ocean. Sci.* **10**, 547–557 (2014).
38. von Schuckmann, K., Cheng, L., Palmer, M. D., Hansen, J. & Tassone, C. Heat stored in the Earth system: where does the energy go? *Earth Syst. Sci. Data* https://doi.org/10.5194/essd-2019-255 (2020).
39. Savita, A. et al. Quantifying spread in spatiotemporal changes of upper-ocean heat content estimates: an internationally coordinated comparison. *J. Clim.* **35**, 851–875 (2022).
40. Le Reste, S. et al. 'Deep-Arvor': a new profiling float to extend the argo observations down to 4000-m depth. *J. Atmos. Ocean. Technol.* **33**, 1039–1055 (2016).
41. Wunsch, C. & Heimbach, P. Bidecadal thermal changes in the abyssal ocean. *J. Phys. Oceanogr.* **44**, 2013–2030 (2014).
42. Chai, F. et al. Monitoring ocean biogeochemistry with autonomous platforms. *Nat. Rev. Earth Environ.* **1**, 315–326 (2020).
43. Goni, G. J. et al. More than 50 years of successful continuous temperature section measurements by the Global Expendable Bathythermograph Network, its integrability, societal benefits, and future. *Front. Mar. Sci.* **6**, 00452 (2019).
44. McMahon, C. R. et al. Animal borne ocean sensors — AniBOS — an essential component of the global ocean observing system. *Front. Mar. Sci.* **8**, 751840 (2021).
45. Boyer, T. et al. Sensitivity of global upper-ocean heat content estimates to mapping methods, XBT bias corrections, and baseline climatologies. *J. Clim.* **29**, 4817–4842 (2016).
46. Levitus, S., Antonov, J. I., Boyer, T. P. & Stephens, C. Warming of the world ocean. *Science* **287**, 2225–2229 (2000).
47. Ishii, M., Kimoto, M. & Kachi, M. Historical ocean subsurface temperature analysis with error estimates. *Mon. Weather Rev.* **131**, 51–73 (2003).
48. Gouretski, V. & Koltermann, K. P. How much is the ocean really warming? *Geophys. Res. Lett.* https://doi.org/10.1029/2006GL027834 (2007).
49. Gouretski, V. & Cheng, L. Correction for systematic errors in the global dataset of temperature profiles from mechanical bathythermographs. *J. Atmos. Ocean. Technol.* **37**, 841–855 (2020).
50. Willis, J. K., Lyman, J. M., Johnson, G. C. & Gilson, J. Correction to "Recent cooling of the upper ocean". *Geophys. Res. Lett.* https://doi.org/10.1029/2007GL030323 (2007).
51. Lyman, J. M. et al. Robust warming of the global upper ocean. *Nature* **465**, 334–337 (2010).
52. Lyman, J. M. & Johnson, G. C. Estimating global ocean heat content changes in the upper 1800 m since 1950 and the influence of climatology choice. *J. Clim.* **27**, 1945–1957 (2014).
53. Durack, P. J., Gleckler, P. J., Landerer, F. W. & Taylor, K. E. Quantifying underestimates of long-term upper-ocean warming. *Nat. Clim. Change* **4**, 999–1005 (2014).
54. Wang, G., Cai, W. & Santoso, A. Assessing the impact of model biases on the projected increase in frequency of extreme positive indian ocean dipole events. *J. Clim.* **30**, 2757–2767 (2017).

55. Roemmich, D. & Gilson, J. The 2004–2008 mean and annual cycle of temperature, salinity, and steric height in the global ocean from the Argo Program. *Prog. Oceanogr.* **82**, 81–100 (2009).
56. Hosoda, S., Ohira, T. & Nakamura, T. Monthly mean dataset of global oceanic temperature and salinity derived from Argo float observations. *JAMSTEC Rep. Res. Dev.* **8**, 47 (2008).
57. Cheng, L. & Zhu, J. Artifacts in variations of ocean heat content induced by the observation system changes. *Geophys. Res. Lett.* **41**, 7276–7283 (2014).
58. Rhein, M. et al. in *Climate Change 2013: The Physical Science Basis* (eds Stocker, T. F. et al.) 255–316 (Cambridge Univ. Press, 2013).
59. Cheng, L. et al. Improved estimates of ocean heat content from 1960 to 2015. *Sci. Adv.* **3**, e1601545 (2017).
60. Ishii, M. et al. Accuracy of global upper ocean heat content estimation expected from present observational data sets. *SOLA* **13**, 163–167 (2017).
61. Willis, J. K. Combining altimetric height with broadscale profile data to estimate steric height, heat storage, subsurface temperature, and sea-surface temperature variability. *J. Geophys. Res. Oceans* https://doi.org/10.1029/2002JC001755 (2003).
62. Levitus, S. et al. World ocean heat content and thermosteric sea level change (0–2000 m), 1955–2010. *Geophys. Res. Lett.* **39**, L10603 (2012).
63. Bagnell, A. & DeVries, T. 20th century cooling of the deep ocean contributed to delayed acceleration of Earth's energy imbalance. *Nat. Commun.* **12**, 4604 (2021).
64. Domingues, C. M. et al. Improved estimates of upper-ocean warming and multi-decadal sea-level rise. *Nature* **453**, 1090–1093 (2008).
65. Su, H. et al. OPEN: a new estimation of global ocean heat content for upper 2000 meters from remote sensing data. *Remote Sens* https://doi.org/10.3390/rs12142294 (2020).
66. Hakuba, M. Z., Frederikse, T. & Landerer, F. W. Earth's energy imbalance from the ocean perspective (2005–2019). *Geophys. Res. Lett.* **48**, e2021GL093624 (2021).
67. Marti, F. et al. Monitoring the ocean heat content change and the Earth energy imbalance from space altimetry and space gravimetry. *Earth Syst. Sci. Data* https://doi.org/10.5194/essd-2021-220 (2021).
68. Llovel, W., Willis, J. K., Landerer, F. W. & Fukumori, I. Deep-ocean contribution to sea level and energy budget not detectable over the past decade. *Nat. Clim. Change* **4**, 1031–1035 (2014).
69. Zanna, L., Khatiwala, S., Gregory, J. M., Ison, J. & Heimbach, P. Global reconstruction of historical ocean heat storage and transport. *Proc. Natl Acad. Sci. USA* **116**, 1126–1131 (2019).
70. Gebbie, G. & Huybers, P. The Little Ice Age and 20th-century deep Pacific cooling. *Science* **363**, 70–74 (2019).
71. Storto, A. et al. Ocean reanalyses: recent advances and unsolved challenges. *Front. Mar. Sci* https://doi.org/10.3389/fmars.2019.00418 (2019).
72. Lellouche, J.-M. et al. The Copernicus global 1/12° oceanic and sea ice GLORYS12 reanalysis. *Front. Earth Sci.* **9**, 698876 (2021).
73. Balmaseda, M. A. et al. The Ocean Reanalyses Intercomparison Project (ORA-IP). *J. Oper. Oceanogr.* **8**, s80–s97 (2015).
74. Wunsch, C. Is the ocean speeding up? Ocean surface energy trends. *J. Phys. Oceanogr.* **50**, 3205–3217 (2020).
75. Palmer, M. D. et al. Ocean heat content variability and change in an ensemble of ocean reanalyses. *Clim. Dyn.* **49**, 909–930 (2017).
76. Trenberth, K. E., Fasullo, J. T., von Schuckmann, K. & Cheng, L. Insights into Earth's energy imbalance from multiple sources. *J. Clim.* **29**, 7495–7505 (2016).
77. Balmaseda, M. A., Trenberth, K. E. & Källén, E. Distinctive climate signals in reanalysis of global ocean heat content. *Geophys. Res. Lett.* **40**, 1754–1759 (2013).
78. Penduff, T. et al. Chaotic variability of ocean heat content: climate-relevant features and observational implications. *Oceanography.* **31**, 210 (2018).
79. Cheng, L. et al. Evolution of ocean heat content related to ENSO. *J. Clim.* **32**, 3529–3556 (2019).
80. Roemmich, D. & Gilson, J. The global ocean imprint of ENSO. *Geophys. Res. Lett.* https://doi.org/10.1029/2011GL047992 (2011).
81. Cheng, L., Foster, G., Hausfather, Z., Trenberth, K. E. & Abraham, J. Improved quantification of the rate of ocean warming. *J. Clim.* **35**, 4827–4840 (2022).
82. Gulev, S. et al. in *Climate Change 2021: The Physical Science Basis* (eds Masson-Delmotte, V. et al.) 287–422 (Cambridge Univ. Press, 2021).
83. Johnson, G. C. & Birnbaum, A. N. As El Niño builds, Pacific warm pool expands, ocean gains more heat. *Geophys. Res. Lett.* **44**, 438–445 (2017).
84. Church, J. A., White, N. J. & Arblaster, J. M. Significant decadal-scale impact of volcanic eruptions on sea level and ocean heat content. *Nature* **438**, 74–77 (2005).
85. Gleckler, P. J., Durack, P. J., Stouffer, R. J., Johnson, G. C. & Forest, C. E. Industrial-era global ocean heat uptake doubles in recent decades. *Nat. Clim. Change* **6**, 394–398 (2016).
86. Kramer, R. J. et al. Observational evidence of increasing global radiative forcing. *Geophys. Res. Lett.* **48**, e2020GL091585 (2021).
87. Eyring, V. et al. Overview of the coupled model intercomparison project phase 6 (CMIP6) experimental design and organization. *Geosci. Model. Dev.* **9**, 1937–1958 (2016).
88. Gleckler, P. J. et al. Human-induced global ocean warming on multidecadal timescales. *Nat. Clim. Change* **2**, 524–529 (2012).
89. Barnett, T. P. et al. Penetration of human-induced warming into the world's oceans. *Science* **309**, 284–287 (2005).
90. Bilbao, R. A. F., Gregory, J. M., Bouttes, N., Palmer, M. D. & Stott, P. Attribution of ocean temperature change to anthropogenic and natural forcings using the temporal, vertical and geographical structure. *Clim. Dyn.* **53**, 5389–5413 (2019).
91. Tokarska, K. B., Hegerl, G. C., Schurer, A. P., Ribes, A. & Fasullo, J. T. Quantifying human contributions to past and future ocean warming and thermosteric sea level rise. *Environ. Res. Lett.* **14**, 074020 (2019).
92. Tokarska, K. B. et al. Past warming trend constrains future warming in CMIP6 models. *Sci. Adv.* **6**, eaaz9549 (2020).
93. Silvy, Y., Guilyardi, E., Sallée, J.-B. & Durack, P. J. Human-induced changes to the global ocean water masses and their time of emergence. *Nat. Clim. Change* **10**, 1030–1036 (2020).
94. Raghuraman, S. P., Paynter, D. & Ramaswamy, V. Anthropogenic forcing and response yield observed positive trend in Earth's energy imbalance. *Nat. Commun.* **12**, 4577 (2021).
95. Gebbie, G. Combining modern and paleoceanographic perspectives on ocean heat uptake. *Annu. Rev. Mar. Sci.* **13**, 255–281 (2021).
96. Purkey, S. G. & Johnson, G. C. Warming of global abyssal and deep southern ocean waters between the 1990s and 2000s: contributions to global heat and sea level rise budgets. *J. Clim.* **23**, 6336–6351 (2010).
97. Desbruyères, D., McDonagh, E. L., King, B. A. & Thierry, V. Global and full-depth ocean temperature trends during the early twenty-first century from Argo and repeat hydrography. *J. Clim.* **30**, 1985–1997 (2017).
98. Storto, A., Cheng, L. & Yang, C. Revisiting the 2003–2018 deep-ocean warming through multi-platform analysis of the global energy budget. *J. Clim.* **35**, 4701–4717 (2022).
99. Sohail, T., Irving, D. B., Zika, J. D., Holmes, R. M. & Church, J. A. Fifty year trends in global ocean heat content traced to surface heat fluxes in the sub-polar ocean. *Geophys. Res. Lett.* **48**, e2020GL091439 (2021).
100. Cheng, L. et al. XBT science: assessment of instrumental biases and errors. *Bull. Am. Meteorol. Soc.* **97**, 924–933 (2016).
101. Cheng, L. et al. How well can we correct systematic errors in historical XBT data? *J. Atmos. Ocean. Technol.* **35**, 1103–1125 (2018).
102. Dangendorf, S. et al. Data-driven reconstruction reveals large-scale ocean circulation control on coastal sea level. *Nat. Clim. Change* **11**, 514–520 (2021).
103. Bullister, J. L., Rhein, M. & Mauritzen, C. in *International Geophysics* Vol. 103 (eds Siedler, G. et al.) 227–253 (Academic, 2013).
104. Cornwall, W. A new 'Blob' menaces Pacific ecosystems. *Science* **365**, 1233–1233 (2019).
105. Piatt, J. F. et al. Extreme mortality and reproductive failure of common murres resulting from the northeast Pacific marine heatwave of 2014–2016. *PLoS One* **15**, e0226087 (2020).
106. Mayer, M., Haimberger, L. & Balmaseda, M. A. On the energy exchange between tropical ocean basins related to ENSO. *J. Clim.* **27**, 6393–6403 (2014).
107. Mayer, M., Alonso Balmaseda, M. & Haimberger, L. Unprecedented 2015/2016 Indo-Pacific heat transfer speeds up tropical pacific heat recharge. *Geophys. Res. Lett.* **45**, 3274–3284 (2018).
108. Wu, Q., Zhang, X., Church, J. A. & Hu, J. ENSO-related global ocean heat content variations. *J. Clim.* **32**, 45–68 (2019).
109. Roemmich, D. et al. Unabated planetary warming and its ocean structure since 2006. *Nat. Clim. Change* **5**, 240–245 (2015).
110. Kosaka, Y. & Xie, S.-P. Recent global-warming hiatus tied to equatorial Pacific surface cooling. *Nature* **501**, 403–407 (2013).
111. Meehl, G. A., Teng, H., Capotondi, A. & Hu, A. The role of interannual ENSO events in decadal timescale transitions of the interdecadal Pacific oscillation. *Clim. Dyn.* **57**, 1933–1951 (2021).
112. Wu, B., Lin, X. & Yu, L. North Pacific subtropical mode water is controlled by the Atlantic multidecadal variability. *Nat. Clim. Change* **10**, 238–243 (2020).
113. Sun, C. et al. Western tropical Pacific multidecadal variability forced by the Atlantic multidecadal oscillation. *Nat. Commun.* **8**, 15998 (2017).
114. Wu, B., Lin, X. & Yu, L. Decadal to multidecadal variability of the mixed layer to the south of the Kuroshio Extension Region. *J. Clim.* **33**, 7697–7714 (2020).
115. England, M. H. et al. Recent intensification of wind-driven circulation in the Pacific and the ongoing warming hiatus. *Nat. Clim. Change* **4**, 222–227 (2014).
116. Douville, H., Voldoire, A. & Geoffroy, O. The recent global warming hiatus: what is the role of Pacific variability? *Geophys. Res. Lett.* **42**, 880–888 (2015).
117. Sprintall, J. et al. Detecting change in the Indonesian seas. *Front. Mar. Sci.* **6**, 257 (2019).
118. England, M. H. & Huang, F. On the interannual variability of the Indonesian throughflow and its linkage with ENSO. *J. Clim.* **18**, 1435–1444 (2005).
119. Trenberth, K. E. & Zhang, Y. Observed interhemispheric meridional heat transports and the role of the Indonesian throughflow in the Pacific ocean. *J. Clim.* **32**, 8523–8536 (2019).
120. Maher, N., England, M. H., Gupta, A. S. & Spence, P. Role of Pacific trade winds in driving ocean temperatures during the recent slowdown and projections under a wind trend reversal. *Clim. Dyn.* **51**, 321–336 (2018).
121. Gong, Z. et al. An inter-basin teleconnection from the North Atlantic to the subarctic North Pacific at multidecadal time scales. *Clim. Dyn.* **54**, 807–822 (2020).
122. Wu, B., Lin, X. & Qiu, B. Meridional shift of the Oyashio extension front in the past 36 years. *Geophys. Res. Lett.* **45**, 9042–9048 (2018).
123. Yang, H. et al. Poleward shift of the major ocean gyres detected in a warming climate. *Geophys. Res. Lett.* **47**, e2019GL085868 (2020).
124. von Schuckmann, K. et al. Copernicus marine service ocean state report. *J. Oper. Oceanogr.* **11**, S1–S142 (2018).
125. Zika, J. D., Gregory, J. M., McDonagh, E. L., Marzocchi, A. & Clément, L. Recent water mass changes reveal mechanisms of ocean warming. *J. Clim.* **34**, 3461–3479 (2021).
126. Rahmstorf, S. et al. Exceptional twentieth-century slowdown in Atlantic Ocean overturning circulation. *Nat. Clim. Change* **5**, 475–480 (2015).
127. Gregory, J. M. et al. The flux-anomaly-forced model intercomparison project (FAFMIP) contribution to CMIP6: investigation of sea-level and ocean climate change in response to $CO_2$ forcing. *Geosci. Model. Dev.* **9**, 3993–4017 (2016).
128. Jackson, L. C. et al. The evolution of the North Atlantic Meridional Overturning Circulation since 1980. *Nat. Rev. Earth Environ.* **3**, 241–254 (2022).
129. Zhang, R. Coherent surface-subsurface fingerprint of the Atlantic Meridional Overturning Circulation. *Geophys. Res. Lett.* https://doi.org/10.1029/2008GL035463 (2008).
130. Caesar, L., Rahmstorf, S., Robinson, A., Feulner, G. & Saba, V. Observed fingerprint of a weakening Atlantic Ocean overturning circulation. *Nature* **556**, 191–196 (2018).
131. Cunningham, S. A. et al. Temporal variability of the Atlantic Meridional Overturning Circulation at 26.5 degrees N. *Science* **317**, 935–938 (2007).
132. Bryden, H. L. et al. Reduction in ocean heat transport at 26°N since 2008 cools the eastern subpolar gyre of the North Atlantic Ocean. *J. Clim.* **33**, 1677–1689 (2020).
133. Trenberth, K. E., Zhang, Y., Fasullo, J. T. & Cheng, L. Observation-based estimates of global and basin ocean meridional heat transport time series. *J. Clim.* **32**, 4567–4583 (2019).
134. Fu, Y., Li, F., Karstensen, J. & Wang, C. A stable Atlantic Meridional Overturning Circulation in a changing north atlantic ocean since the 1990s. *Sci. Adv.* **6**, eabc7836 (2020).

135. Cimatoribus, A., van Oldenborgh, G. J. & Drijfhout, S. Is a decline of AMOC causing the warming hole above the North Atlantic in observed and modeled warming patterns? *J. Clim.* **25**, 8373–8379 (2012).
136. Gervais, M., Shaman, J. & Kushnir, Y. Mechanisms governing the development of the North Atlantic warming hole in the CESM-LE future climate simulations. *J. Clim.* **31**, 5927–5946 (2018).
137. Gu, S., Liu, Z. & Wu, L. Time scale dependence of the meridional coherence of the Atlantic Meridional Overturning Circulation. *J. Geophys. Res. Oceans* **125**, e2019JC015838 (2020).
138. Clement, A. et al. The Atlantic multidecadal oscillation without a role for ocean circulation. *Science* **350**, 320–324 (2015).
139. Woollings, T., Gregory, J. M., Pinto, J. G., Reyers, M. & Brayshaw, D. J. Response of the North Atlantic storm track to climate change shaped by ocean–atmosphere coupling. *Nat. Geosci.* **5**, 313–317 (2012).
140. Feser, F. et al. Storminess over the North Atlantic and northwestern Europe — a review. *Q. J. R. Meteorol. Soc.* **141**, 350–382 (2015).
141. Li, L., Lozier, M. S. & Li, F. Century-long cooling trend in subpolar North Atlantic forced by atmosphere: an alternative explanation. *Clim. Dyn.* **58**, 2249–2267 (2021).
142. Josey, S. A. et al. The recent atlantic cold anomaly: causes, consequences, and related phenomena. *Annu. Rev. Mar. Sci.* **10**, 475–501 (2018).
143. Delworth, T. L. et al. The North Atlantic Oscillation as a driver of rapid climate change in the Northern Hemisphere. *Nat. Geosci.* **9**, 509–512 (2016).
144. Stepanov, V. N. & Haines, K. Mechanisms of Atlantic Meridional Overturning Circulation variability simulated by the NEMO model. *Ocean. Sci.* **10**, 645–656 (2014).
145. Hu, S. & Fedorov, A. V. Indian Ocean warming as a driver of the North Atlantic warming hole. *Nat. Commun.* **11**, 4785 (2020).
146. Li, Y., Han, W., Hu, A., Meehl, G. A. & Wang, F. Multidecadal changes of the Upper Indian Ocean heat content during 1965–2016. *J. Clim.* **31**, 7863–7884 (2018).
147. Ummenhofer, C. C., Murty, S. A., Sprintall, J., Lee, T. & Abram, N. J. Heat and freshwater changes in the Indian Ocean region. *Nat. Rev. Earth Environ.* **2**, 525–541 (2021).
148. Lee, S.-K. et al. Pacific origin of the abrupt increase in Indian Ocean heat content during the warming hiatus. *Nat. Geosci.* **8**, 445–449 (2015).
149. Li, Y., Han, W., Wang, F., Zhang, L. & Duan, J. Vertical structure of the Upper-Indian Ocean thermal variability. *J. Clim.* **33**, 7233–7253 (2020).
150. Volkov, D. L., Lee, S.-K., Gordon, A. L. & Rudko, M. Unprecedented reduction and quick recovery of the South Indian Ocean heat content and sea level in 2014. *Sci. Adv.* **6**, eabc1151 (2020).
151. Liu, Q., Feng, M., Wang, D. & Wijffels, S. Interannual variability of the Indonesian throughflow transport: a revisit based on 30 year expendable bathythermograph data. *J. Geophys. Res. Oceans* **120**, 8270–8282 (2015).
152. Yang, L., Murtugudde, R., Zhou, L. & Liang, P. A potential link between the Southern Ocean warming and the South Indian Ocean heat balance. *J. Geophys. Res. Oceans* **125**, e2020JC016132 (2020).
153. Duan, J. et al. Rapid sea-level rise in the Southern-Hemisphere subtropical Oceans. *J. Clim.* https://doi.org/10.1175/JCLI-D-21-0248.1 (2021).
154. Hong, Y., Du, Y., Qu, T., Zhang, Y. & Cai, W. Variability of the Subantarctic mode water volume in the South Indian Ocean during 2004–2018. *Geophys. Res. Lett.* **47**, e2020GL087830 (2020).
155. Sallée, J.-B. Southern Ocean warming. *Oceanography* **31**, 52–62 (2018).
156. Frölicher, T. L. et al. Dominance of the Southern Ocean in anthropogenic carbon and heat uptake in CMIP5 models. *J. Clim.* **28**, 862–886 (2015).
157. Gille, S. T. Warming of the Southern Ocean since the 1950s. *Science* **295**, 1275–1277 (2002).
158. Purich, A., Cai, W., England, M. H. & Cowan, T. Evidence for link between modelled trends in Antarctic sea ice and underestimated westerly wind changes. *Nat. Commun.* **7**, 10409 (2016).
159. Meredith, M. et al. in *Special Report on the Ocean and Cryosphere in a Changing Climate* (eds Pörtner, H.-O. et al.) Ch. 3 (IPCC, 2019).
160. Swart, N. C., Gille, S. T., Fyfe, J. C. & Gillett, N. P. Recent Southern Ocean warming and freshening driven by greenhouse gas emissions and ozone depletion. *Nat. Geosci.* **11**, 836–841 (2018).
161. Eyring, V. et al. Reflections and projections on a decade of climate science. *Nat. Clim. Change* **11**, 279–285 (2021).
162. Cai, W., Cowan, T., Godfrey, S. & Wijffels, S. Simulations of processes associated with the fast warming rate of the Southern Midlatitude Ocean. *J. Clim.* **23**, 197–206 (2010).
163. Armour, K. C., Marshall, J., Scott, J. R., Donohoe, A. & Newsom, E. R. Southern Ocean warming delayed by circumpolar upwelling and equatorward transport. *Nat. Geosci.* **9**, 549–554 (2016).
164. Gao, L., Rintoul, S. R. & Yu, W. Recent wind-driven change in Subantarctic mode water and its impact on ocean heat storage. *Nat. Clim. Change* **8**, 58–63 (2017).
165. Li, Z., England, M. H., Groeskamp, S., Cerovečki, I. & Luo, Y. The origin and fate of Subantarctic mode water in the Southern Ocean. *J. Phys. Oceanogr.* **51**, 2951–2972 (2021).
166. Huguenin, M. F., Holmes, R. M. & England, M. H. Drivers and distribution of global ocean heat uptake over the last half century. *Nat. Commun.* **13**, 4921 (2022).
167. Purich, A., England, M. H., Cai, W., Sullivan, A. & Durack, P. J. Impacts of broad-scale surface freshening of the southern ocean in a coupled climate model. *J. Clim.* **31**, 2613–2632 (2018).
168. Hyder, P. et al. Critical Southern Ocean climate model biases traced to atmospheric model cloud errors. *Nat. Commun.* **9**, 3625 (2018).
169. Schuddeboom, A. J. & McDonald, A. J. The Southern Ocean radiative bias, cloud compensating errors, and equilibrium climate sensitivity in CMIP6 models. *J. Geophys. Res. Atmos.* **126**, e2021JD035310 (2021).
170. Munday, D. R., Johnson, H. L. & Marshall, D. P. Eddy saturation of equilibrated circumpolar currents. *J. Phys. Oceanogr.* **43**, 507–532 (2013).
171. Hogg, A. M. et al. Recent trends in the Southern Ocean eddy field. *J. Geophys. Res. Oceans* **120**, 257–267 (2015).
172. Patara, L., Böning, C. W. & Biastoch, A. Variability and trends in Southern Ocean eddy activity in 1/12° ocean model simulations. *Geophys. Res. Lett.* **43**, 4517–4523 (2016).
173. Wu, L., Jing, Z., Riser, S. & Visbeck, M. Seasonal and spatial variations of Southern Ocean diapycnal mixing from Argo profiling floats. *Nat. Geosci.* **4**, 363–366 (2011).
174. Shi, J.-R., Talley, L. D., Xie, S.-P., Peng, Q. & Liu, W. Ocean warming and accelerating Southern Ocean zonal flow. *Nat. Clim. Change* **11**, 1090–1097 (2021).
175. Pellichero, V., Sallee, J. B., Chapman, C. C. & Downes, S. M. The southern ocean meridional overturning in the sea-ice sector is driven by freshwater fluxes. *Nat. Commun.* **9**, 1789 (2018).
176. Haumann, F. A., Gruber, N. & Münnich, M. Sea-ice induced Southern Ocean subsurface warming and surface cooling in a warming climate. *AGU Adv.* **1**, e2019AV000132 (2020).
177. Meehl, G. A. et al. Sustained ocean changes contributed to sudden Antarctic sea ice retreat in late 2016. *Nat. Commun.* **10**, 14 (2019).
178. Li, X. et al. Tropical teleconnection impacts on Antarctic climate changes. *Nat. Rev. Earth Environ.* **2**, 680–698 (2021).
179. Wu, L. et al. Enhanced warming over the global subtropical western boundary currents. *Nat. Clim. Change* **2**, 161–166 (2012).
180. Duran, E. R., England, M. H. & Spence, P. Surface ocean warming around Australia driven by interannual variability and long-term trends in Southern Hemisphere westerlies. *Geophys. Res. Lett.* **47**, e2019GL086605 (2020).
181. Lago, V. & England, M. H. Projected slowdown of Antarctic bottom water formation in response to amplified meltwater contributions. *J. Clim.* **32**, 6319–6335 (2019).
182. MedECC in *Climate and Environmental Change in the Mediterranean Basin: Current Situation and Risks for the Future.* First Mediterranean Assessment Report (eds Cramer, W., Guiot, J. & Marini, K.) 11–40 (Union for the Mediterranean, Plan Bleu, UNEP/MAP, 2020).
183. Pinardi, N. et al. Mediterranean Sea large-scale low-frequency ocean variability and water mass formation rates from 1987 to 2007: a retrospective analysis. *Prog. Oceanogr.* **132**, 318–332 (2015).
184. Masina, S. et al. The North Atlantic–Mediterranean overturning systems teleconnection. In *Copernicus Ocean State Report. J. Oceanogr.* (in the press).
185. Pinardi, N., Cessi, P., Borile, F. & Wolfe, C. L. P. The Mediterranean sea overturning circulation. *J. Phys. Oceanogr.* **49**, 1699–1721 (2019).
186. Jordà, G. et al. The Mediterranean Sea heat and mass budgets: estimates, uncertainties and perspectives. *Prog. Oceanogr.* **156**, 174–208 (2017).
187. Lionello, P. et al. The climate of the Mediterranean region: research progress and climate change impacts. *Reg. Environ. Change* **14**, 1679–1684 (2014).
188. Schroeder, K. et al. Rapid response to climate change in a marginal sea. *Sci. Rep.* **7**, 4065 (2017).
189. Simoncelli, S., Fratianni, C. & Mattia, G. Monitoring and long-term assessment of the Mediterranean Sea physical state through ocean reanalyses. In *INGV Workshop on Marine Environment Abstract Volume* (eds. Sagnotti, L. et al.) Misc. INGV, 51: 1126 (INGV, 2019).
190. Zunino, P. et al. Effects of the Western Mediterranean transition on the resident water masses: pure warming, pure freshening and pure heaving. *J. Mar. Syst.* **96–97**, 15–23 (2012).
191. Simoncelli, S., Pinardi, N., Fratianni, C., Dubois, C. & Notarstefano, G. Water mass formation processes in the Mediterranean Sea over the past 30 years. In *Copernicus Marine Service Ocean State Report*, Issue 2. *J. Oper. Oceanogr.* **11**, s1–s142 (2018).
192. Sammartino, S., Lafuente, J., Naranjo, C. & Simoncelli, S. Ventilation of the western Mediterranean deep water through the strait of Gibraltar. In *Copernicus Marine Service Ocean State Report*, Issue 2. *J. Oper. Oceanogr.* **11**, s13–s16 (2018).
193. Cherif, S. et al. in *Climate and Environmental Change in the Mediterranean Basin: Current Situation and Risks for the Future.* First Mediterranean Assessment Report (eds. Cramer, W., Guiot, J. & Marini, K.) 59–180 (Union for the Mediterranean, Plan Bleu, UNEP/MAP, 2020).
194. Mayer, M. et al. Atmospheric and oceanic contributions to observed Nordic Seas and Arctic Ocean heat content variations 1993–2020. In *Copernicus Marine Service Ocean State Report. J. Oper. Oceanogr.* (in the press).
195. Polyakov, I. V. et al. Greater role for Atlantic inflows on sea-ice loss in the Eurasian Basin of the Arctic Ocean. *Science* **356**, 285–291 (2017).
196. Ingvaldsen, R. B. et al. Physical manifestations and ecological implications of Arctic Atlantification. *Nat. Rev. Earth Environ.* **2**, 874–889 (2021).
197. Tesi, T. et al. Rapid Atlantification along the Fram Strait at the beginning of the 20th century. *Sci. Adv.* **7**, eabj2946 (2021).
198. Spooner, P. T. et al. Exceptional 20th century ocean circulation in the Northeast Atlantic. *Geophys. Res. Lett.* **47**, e2020GL087577 (2020).
199. Caesar, L., McCarthy, G. D., Thornalley, D. J. R., Cahill, N. & Rahmstorf, S. Current Atlantic Meridional Overturning Circulation weakest in last millennium. *Nat. Geosci.* **14**, 118–120 (2021).
200. Li, F. et al. Subpolar North Atlantic western boundary density anomalies and the Meridional Overturning Circulation. *Nat. Commun.* **12**, 3002 (2021).
201. Tsubouchi, T. et al. Increased ocean heat transport into the Nordic Seas and Arctic Ocean over the period 1993–2016. *Nat. Clim. Change* **11**, 21–26 (2021).
202. Fox-Kemper, B. et al. in *Climate Change 2021: The Physical Science Basis* (eds Masson-Delmotte, V. et al.) 1211–1361 (Cambridge Univ. Press, 2021).
203. Winton, M., Takahashi, K. & Held, I. M. Importance of ocean heat uptake efficacy to transient climate change. *J. Clim.* **23**, 2333–2344 (2010).
204. Marshall, J. et al. The ocean's role in the transient response of climate to abrupt greenhouse gas forcing. *Clim. Dyn.* **44**, 2287–2299 (2014).
205. Lyu, K., Zhang, X. & Church, J. A. Projected ocean warming constrained by the ocean observational record. *Nat. Clim. Change* **11**, 834–839 (2021).
206. Hansen, J. et al. Climate response times: dependence on climate sensitivity and ocean mixing. *Science* **229**, 857–859 (1985).
207. Rose, B. E. J. & Rayborn, L. The effects of ocean heat uptake on transient climate sensitivity. *Curr. Clim. Change Rep.* **2**, 190–201 (2016).
208. Hawkins, E., Smith, R. S., Gregory, J. M. & Stainforth, D. A. Irreducible uncertainty in near-term climate projections. *Clim. Dyn.* **46**, 3807–3819 (2016).
209. Bonnet, R. et al. Increased risk of near term global warming due to a recent AMOC weakening. *Nat. Commun.* **12**, 6108 (2021).
210. Nowicki, S. et al. Experimental protocol for sea level projections from ISMIP6 stand-alone ice sheet models. *Cryosphere* **14**, 2331–2368 (2020).

211. Mann, M. E. Beyond the hockey stick: climate lessons from the Common Era. *Proc. Natl Acad. Sci. USA* **118**, e2112797118 (2021).
212. Irving, D., Hobbs, W., Church, J. & Zika, J. A mass and energy conservation analysis of drift in the CMIP6 ensemble. *J. Clim.* **34**, 3157–3170 (2020).
213. Luyten, J., Pedlosky, J. & Stommel, H. The ventilated thermocline. *J. Phys. Oceanogr.* **13**, 292–309 (1983).
214. Seager, R., Henderson, N. & Cane, M. Persistent discrepancies between observed and modeled trends in the tropical Pacific Ocean. *J. Clim.* **35**, 4571–4584 (2022).
215. Wengel, C. et al. Future high-resolution El Niño/Southern Oscillation dynamics. *Nat. Clim. Change* **11**, 758–765 (2021).
216. Shi, J.-R., Xie, S.-P. & Talley, L. D. Evolving relative importance of the Southern Ocean and North Atlantic in Anthropogenic Ocean heat uptake. *J. Clim.* **31**, 7459–7479 (2018).
217. Irving, D. B., Wijffels, S. & Church, J. A. Anthropogenic aerosols, greenhouse gases, and the uptake, transport, and storage of excess heat in the climate system. *Geophys. Res. Lett.* **46**, 4894–4903 (2019).
218. Sloyan, B. M. & Rintoul, S. R. Circulation, renewal, and modification of Antarctic mode and intermediate water. *J. Phys. Oceanogr.* **31**, 1005–1030 (2001).
219. Purkey, S. G. & Johnson, G. C. Antarctic bottom water warming and freshening: contributions to sea level rise, ocean freshwater budgets, and global heat gain. *J. Clim.* **26**, 6105–6122 (2013).
220. Liu, W., Lu, J., Xie, S.-P. & Fedorov, A. Southern ocean heat uptake, redistribution, and storage in a warming climate: the role of meridional overturning circulation. *J. Clim.* **31**, 4727–4743 (2018).
221. Soto-Navarro, J. et al. Evolution of Mediterranean sea water properties under climate change scenarios in the Med-CORDEX ensemble. *Clim. Dyn.* **54**, 2135–2165 (2020).
222. Somot, S., Sevault, F. & Déqué, M. Transient climate change scenario simulation of the Mediterranean Sea for the twenty-first century using a high-resolution ocean circulation model. *Clim. Dyn.* **27**, 851–879 (2006).
223. Carillo, A. et al. Steric sea level rise over the Mediterranean sea: present climate and scenario simulations. *Clim. Dyn.* **39**, 2167–2184 (2012).
224. Khosravi, N. et al. The Arctic Ocean in CMIP6 models: biases and projected changes in temperature and salinity. *Earths Future* **10**, e2021EF002282 (2021).
225. Roberts, C. D. et al. Surface flux and ocean heat transport convergence contributions to seasonal and interannual variations of ocean heat content. *J. Geophys. Res. Oceans* **122**, 726–744 (2017).
226. Marshall, D. P. & Zanna, L. A conceptual model of ocean heat uptake under climate change. *J. Clim.* **27**, 8444–8465 (2014).
227. Kostov, Y., Armour, K. C. & Marshall, J. Impact of the Atlantic Meridional Overturning Circulation on ocean heat storage and transient climate change. *Geophys. Res. Lett.* **41**, 2108–2116 (2014).
228. Todd, A. et al. Ocean-only FAFMIP: understanding regional patterns of ocean heat content and dynamic sea level change. *J. Adv. Model. Earth Syst.* **12**, e2019MS002027 (2020).
229. Couldrey, M. et al. What causes the spread of model projections of ocean dynamic sea level change in response to greenhouse gas forcing? *Clim. Dyn.* **56**, 155–187 (2021).
230. Dias, F. B. et al. Ocean heat storage in response to changing ocean circulation processes. *J. Clim.* **33**, 9065–9082 (2020).
231. Williams, R. G., Katavouta, A. & Roussenov, V. Regional asymmetries in ocean heat and carbon storage due to dynamic redistribution in climate model projections. *J. Clim.* **34**, 3907–3925 (2021).
232. Wahl, T. & Plant, N. G. Changes in erosion and flooding risk due to long-term and cyclic oceanographic trends. *Geophys. Res. Lett.* **42**, 2943–2950 (2015).
233. Irrgang, A. M. et al. Drivers, dynamics and impacts of changing Arctic coasts. *Nat. Rev. Earth Environ.* **3**, 39–54 (2022).
234. Li, G. et al. Increasing ocean stratification over the past half-century. *Nat. Clim. Change* **10**, 1116–1123 (2020).
235. Breitburg, D. et al. Declining oxygen in the global ocean and coastal waters. *Science* **359**, eaam7240 (2018).
236. Gruber, N., Boyd, P. W., Frolicher, T. L. & Vogt, M. Biogeochemical extremes and compound events in the ocean. *Nature* **600**, 395–407 (2021).
237. Frölicher, T. L., Fischer, E. M. & Gruber, N. Marine heatwaves under global warming. *Nature* **560**, 360–364 (2018).
238. Smale, D. A. et al. Marine heatwaves threaten global biodiversity and the provision of ecosystem services. *Nat. Clim. Change* **9**, 306–312 (2019).
239. Bopp, L. et al. Multiple stressors of ocean ecosystems in the 21st century: projections with CMIP5 models. *Biogeosciences* **10**, 6225–6245 (2013).
240. Steinacher, M. et al. Projected 21st century decrease in marine productivity: a multi-model analysis. *Biogeosciences* **7**, 979–1005 (2010).
241. Ranasinghe, R. et al. in *Climate Change 2021: The Physical Science Basis* (eds Masson-Delmotte, V. et al.) 1767–1926 (Cambridge Univ. Press, 2021).
242. Lam, V. W. Y. et al. Climate change, tropical fisheries and prospects for sustainable development. *Nat. Rev. Earth Environ.* **1**, 440–454 (2020).
243. Mignot, A. et al. Decrease in air–sea $CO_2$ fluxes caused by persistent marine heatwaves. *Nat. Commun.* **13**, 4300 (2022).
244. Gattuso, J.-P. et al. Contrasting futures for ocean and society from different anthropogenic $CO_2$ emissions scenarios. *Science* **349**, aac4722 (2015).
245. Ramírez, F., Afán, I., Davis, L. S. & Chiaradia, A. Climate impacts on global hot spots of marine biodiversity. *Sci. Adv.* **3**, e1601198 (2017).
246. Oliver, E. C. J. et al. The unprecedented 2015/16 Tasman Sea marine heatwave. *Nat. Commun.* **8**, 16101 (2017).
247. Collins, M. et al. Extremes, abrupt changes and managing risk. In *Special Report on the Ocean and Cryosphere in a Changing Climate* (eds Pörtner, H.-O. et al.) 589–632 (IPCC, 2019).
248. Hoegh-Guldberg, O. et al. in *Special Report on Global Warming of 1.5 °C* (eds Masson-Delmotte, V. et al.) 175–284 (IPCC, WMO, 2018).
249. Trenberth, K. E., Cheng, L., Jacobs, P., Zhang, Y. & Fasullo, J. Hurricane Harvey links to ocean heat content and climate change adaptation. *Earths Future* **6**, 730–744 (2018).
250. Barnard, P. L. et al. Coastal vulnerability across the Pacific dominated by El Niño/Southern Oscillation. *Nat. Geosci.* **8**, 801–807 (2015).
251. Cai, W. et al. Increased variability of eastern Pacific El Nino under greenhouse warming. *Nature* **564**, 201–206 (2018).
252. Jacobs, S. S., Giulivi, C. F. & Mele, P. A. Freshening of the Ross Sea during the late 20th century. *Science* **297**, 386–389 (2002).
253. Pritchard, H. D. et al. Antarctic ice-sheet loss driven by basal melting of ice shelves. *Nature* **484**, 502–505 (2012).
254. Shepherd, A. et al. Mass balance of the Antarctic ice sheet from 1992 to 2017. *Nature* **558**, 219–222 (2018).
255. Gardner, A. S. et al. A reconciled estimate of glacier contributions to sea level rise: 2003 to 2009. *Science* **340**, 852–857 (2013).
256. Lenton, T. M. et al. Tipping elements in the Earth's climate system. *Proc. Natl Acad. Sci. USA* **105**, 1786–1793 (2008).
257. Heinze, C. et al. ESD reviews: climate feedbacks in the Earth system and prospects for their evaluation. *Earth Syst. Dynam.* **10**, 379–452 (2019).
258. Hoegh-Guldberg, O., Kennedy, E. V., Beyer, H. L., McClennen, C. & Possingham, H. P. Securing a long-term future for coral reefs. *Trends Ecol. Evol.* **33**, 936–944 (2018).
259. Zilberman, N. V., Roemmich, D. H. & Gilson, J. Deep-ocean circulation in the southwest Pacific Ocean interior: estimates of the mean flow and variability using deep argo data. *Geophys. Res. Lett.* **47**, e2020GL088342 (2020).
260. Roemmich, D. et al. On the future of Argo: a global, full-depth, multi-disciplinary array. *Front. Mar. Sci.* **6**, 439 (2019).
261. Le Traon, P.-Y. et al. Preparing the new phase of Argo: scientific achievements of the NAOS project. *Front. Mar. Sci.* **7**, 577408 (2020).
262. Gasparin, F., Hamon, M., Rémy, E. & Le Traon, P.-Y. How Deep Argo will improve the deep ocean in an ocean reanalysis. *J. Clim.* **33**, 77–94 (2020).
263. Allison, L. C. et al. Towards quantifying uncertainty in ocean heat content changes using synthetic profiles. *Environ. Res. Lett.* **14**, ab2b0b (2019).
264. Llovel, W. et al. Imprint of intrinsic ocean variability on decadal trends of regional sea level and ocean heat content using synthetic profiles. *Environ. Res. Lett.* **17**, 044063 (2022).
265. Danabasoglu, G. et al. Variability of the Atlantic Meridional Overturning Circulation in CCSM4. *J. Clim.* **25**, 5153–5172 (2012).
266. Purich, A. & England, M. H. Historical and future projected warming of Antarctic shelf bottom water in CMIP6 models. *Geophys. Res. Lett.* **48**, e2021GL092752 (2021).
267. Baggenstos, D. et al. Earth's radiative imbalance from the Last Glacial Maximum to the present. *Proc. Natl Acad. Sci. USA* **116**, 14881–14886 (2019).
268. Elderfield, H. et al. Evolution of ocean temperature and ice volume through the mid-Pleistocene climate transition. *Science* **337**, 704–709 (2012).
269. Li, H. et al. Development of a global gridded Argo data set with Barnes successive corrections. *J. Geophys. Res. Oceans* **122**, 866–889 (2017).
270. Allen, M. R. et al. in *Special Report on Global Warming of 1.5 °C* (eds Masson-Delmotte, V. et al.) 49–92 (IPCC, WMO, 2018).
271. Kennedy, J. A review of uncertainty in in situ measurements and data sets of sea surface temperature. *Rev. Geophys.* **52**, 1–32 (2014).
272. O'Carroll, A. G. et al. Observational needs of sea surface temperature. *Front. Mar. Sci.* https://doi.org/10.3389/fmars.2019.00420 (2019).



### Acknowledgements
L.C. acknowledges financial support from the Strategic Priority Research Program of the Chinese Academy of Sciences (XDB42040402), National Natural Science Foundation of China (42122046, 42076202), Youth Innovation Promotion Association, CAS (2020-077). The National Center for Atmospheric Research is sponsored by the US National Science Foundation (NSF). L.Z. is supported by NSF OCE award 2048576. J.F. is supported by NASA awards 80NSSC17K0565 and 80NSSC22K0046, and by the Regional and Global Model Analysis (RGMA) component of the Earth and Environmental System Modeling Program of the US Department of Energy's Office of Biological & Environmental Research (BER) via NSF IA 1947282. M.E. and J.Z. are supported by the Australian Research Council (SR200100008, LP200100406, DP190100494). Y.Y. is supported by National Natural Science Foundation of China (91958201, 42130608). We thank S. Simoncelli for discussion on the Mediterranean Sea, V. Gouretski and F. Reseghetti for discussion on observations. We acknowledge the World Climate Research Programme's Working Group on Coupled Modelling, which is responsible for CMIP, and we thank the climate modelling groups for producing and making available their model output through Earth System Grid Federation. We also acknowledge the International Argo Program and the national programmes that contribute to it. The Argo Program is part of the Global Ocean Observing System.


### Author contributions
All authors contributed to writing and editing the article. L.C., K.v.S., J.P., K.T. and M.M led the overall conceptual design and the activity. L.C. led and coordinated the writing. K.v.S. and L.C. led the Introduction section. J.P.A. and K.v.S. led the observations and OHC estimates section. L.C., K.T., J.Z. and M.E. led the past OHC changes section. L.Z., J. F., M.E., L.C. and Y.-Q.Y. led the future projections section. K.T., L.C. and K.v.S led the impacts and consequences section. L.C., M.M. and K.T. led the final section. Y.-Y.P., J.Z., E.N., B.B., L.P. and L.C. contributed to data processing.

### Competing interests
The authors declare no competing interests.

### Peer review information
*Nature Reviews Earth & Environment* thanks Sarah Purkey and the other, anonymous, reviewer(s) for their contribution to the peer review of this work.

### Publisher's note
Springer Nature remains neutral with regard to jurisdictional claims in published maps and institutional affiliations.



### Supplementary information
The online version contains supplementary material available at https://doi.org/10.1038/s43017-022-00345-1.